LUND UNIVERSITY

From Monte Carlo PET Simulations to Reconstructed Images

Modelling and Optimisation for ^{68}Ga Theragnostics

Kalaitzidis, Philip

2023

Document Version:
Other version

Link to publication

Citation for published version (APA):
Kalaitzidis, P. (2023). *From Monte Carlo PET Simulations to Reconstructed Images: Modelling and Optimisation for ^{68}Ga Theragnostics*. [Doctoral Thesis (compilation), Medical Radiation Physics, Lund]. Tryckeriet i E-huset, Lunds universitet.

Total number of authors:
1

LUND UNIVERSITY

PO Box 117
221 00 Lund
+46 46-222 00 00

From Monte Carlo PET Simulations to Reconstructed Images

Modelling and Optimisation for ^{68}Ga Theragnostics

PHILIP KALAITZIDIS
MEDICAL RADIATION PHYSICS, LUND
FACULTY OF SCIENCE | LUND UNIVERSITY

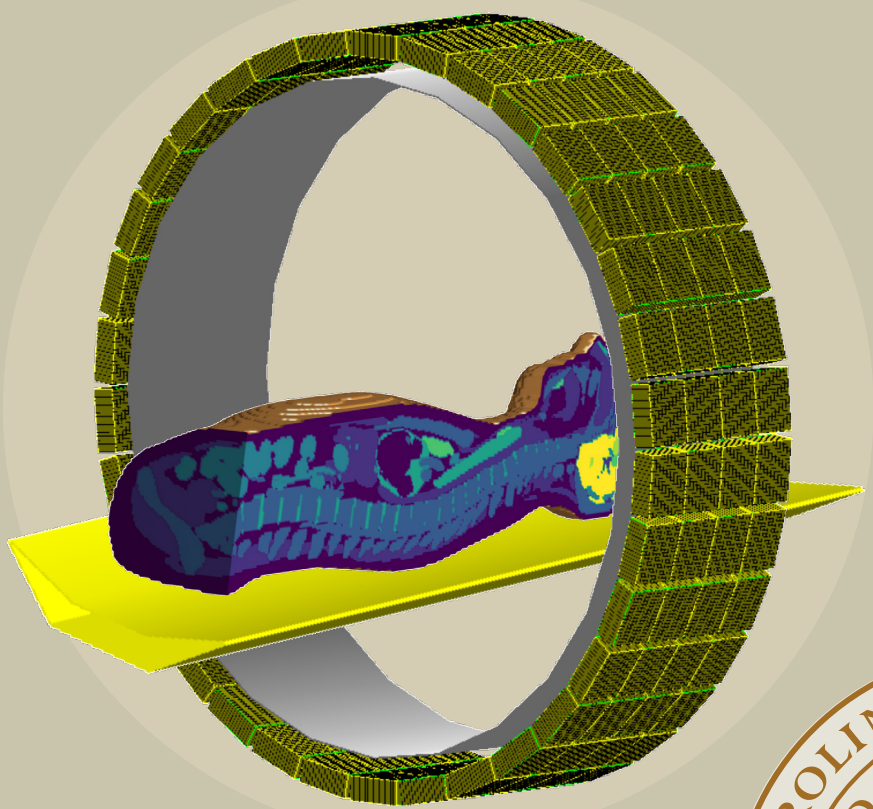

From Monte Carlo PET Simulations to Reconstructed Images

From Monte Carlo PET Simulations to Reconstructed Images

Modelling and Optimisation for ^{68}Ga Theragnostics

Philip Kalaitzidis

LUND
UNIVERSITY

DOCTORAL DISSERTATION
Doctoral dissertation for the degree of Doctor of Philosophy (PhD) at the Faculty of Science at Lund University to be publicly defended on the 01 of December, 2023, 09.00, at Skåne University Hospital, Lund, in lecture hall F1 Blocket.

Faculty opponent
Professor Mark Lubberink
Department of Surgical Sciences, Radiology; Nuclear Medicine and PET, Uppsala University, Sweden.

Organization: LUND UNIVERSITY

Document name: DOCTORAL DISSERTATION **Date of issue:** 2023-11-01

Author(s): Philip Kalaitzidis **Sponsoring organization:**

Title and subtitle: From Monte Carlo PET Simulations to Reconstructed Images: Modelling and Optimisation for ^{68}Ga Theragnostics.

Abstract:

In nuclear medicine, radiopharmaceuticals can be administered for both diagnostic and therapeutic purposes. In recent years, there has been an increasing interest in theragnostics, a strategy that combines both diagnosis and therapy. This can be achieved by using similar radiopharmaceuticals for imaging and radionuclide therapy, which enables highly personalised disease management. One theragnostic application is for the diagnosis and management of neuroendocrine tumours, where the diagnosis and subsequent therapy stratification often relies on a qualitative evaluation following [^{68}Ga]Ga-DOTA-TOC PET imaging, with [^{177}Lu]Lu-DOTA-TATE radionuclide therapy being a potential treatment option. In this case, peri-therapeutic SPECT imaging enables for the disease to be closely monitored during therapy. There is growing interest in utilising quantitative metrics to identify the most suitable candidates for radionuclide therapy and to subsequently perform individualised dosimetry. Consequently, it is important to understand potential limitations in the image acquisition process that will impact the accuracy and precision of quantitative estimates, and one effective method to do so is through Monte Carlo simulations.

This thesis is based on four papers utilising Monte Carlo simulations, with a focus on modelling and optimising for ^{68}Ga-PET theragnostics. Paper I explores the possibility of modelling and simulating a clinical GE Discovery MI PET system and coupling simulated data with a reconstruction software, entirely *in silico*, to enable further simulation-based studies. The implementation of correction factors emulates the process used in clinical scanners for a more realistic approach. The model successfully generates results comparable to those obtained from a corresponding measurement on a clinical scanner. Papers II, III, and IV focus on ^{68}Ga-PET imaging of neuroendocrine tumours, with Papers III and IV also incorporating ^{177}Lu-SPECT imaging. Anthropomorphic phantoms were utilised to enable the simulation of [^{68}Ga]Ga-DOTA-TOC PET and [^{177}Lu]Lu-DOTA-TATE SPECT exams with patient-like geometries and activity distributions. In Paper II, it was shown that a non-linearly scaled administered activity based on patient weight harmonises image quality, regardless of patient body size. A harmonised image quality is important to ensure that all patients receive an equal standard of care. Paper III investigated the potential impact of respiration on quantitative estimates in [^{68}Ga]Ga-DOTA-TOC PET and [^{177}Lu]Lu-DOTA-TATE SPECT imaging. The extent of lesion motion substantially influenced the recovered lesion activity concentration, with deviations exceeding 30% from the simulated activity concentration. Furthermore, differences in quantitative bias were observed between PET and SPECT imaging, primarily attributed to the different imaging time points. In Paper IV, efforts were undertaken to elevate the realism of simulated patient models, enabling the creation of highly realistic simulated images. The ability to generate realistic images holds great future potential, as it allows for the construction of databases of simulated reconstructed images with known ground truth. These databases can serve various purposes, including software performance evaluation and integration with machine learning. In conclusion, the use of a computational pipeline that connects Monte Carlo simulations with a reconstruction software enables simulation-based studies of entire PET-exam procedures to be conducted. Access to the underlying data driving the simulations makes it possible to isolate individual parameters and track their impact on the results, allowing for a systematic evaluation of *in vivo* confounders entirely *in silico*.

Key words: Anthropomorphic phantoms, Monte Carlo modelling, Nuclear medicine, PET, SPECT, Theragnostics, Tomographic Reconstruction

Classification system and/or index terms (if any) Supplementary bibliographical information

Language English **ISSN and key title**:

ISBN: ISBN 978-91-8039-879-4 (print)

ISBN 978-91-8039-878-7 (electronic)

Recipient's notes **Number of pages**: 86

Price Security classification

From Monte Carlo PET Simulations to Reconstructed Images

Modelling and Optimisation for ^{68}Ga Theragnostics

Philip Kalaitzidis

LUND
UNIVERSITY

Coverphoto by Philip Kalaitzidis (Cross-section of an XCAT phantom positioned in a virtual PET scanner).

Faculty of Science, Lund University

Medical Radiation Physics, Lund

ISBN 978-91-8039-879-4 (print)

ISBN 978-91-8039-878-7 (electronic)

Printed in Sweden by Tryckeriet i E-Huset, Lund University

Lund 2023

“Sometimes maybe good,
sometimes maybe shit!”
Gennaro Gattuso

Table of Contents

Summary

In nuclear medicine, radiopharmaceuticals can be administered for both diagnostic and therapeutic purposes. In recent years, there has been an increasing interest in theragnostics, a strategy that combines both diagnosis and therapy. This can be achieved by using similar radiopharmaceuticals for imaging and radionuclide therapy, which enables highly personalised disease management. One theragnostic application is for the diagnosis and management of neuroendocrine tumours, where the diagnosis and subsequent therapy stratification often relies on a qualitative evaluation following [^{68}Ga]Ga-DOTA-TOC PET imaging, with [^{177}Lu]Lu-DOTA-TATE radionuclide therapy being a potential treatment option. In this case, peri-therapeutic SPECT imaging enables for the disease to be closely monitored during therapy. There is growing interest in utilising quantitative metrics to identify the most suitable candidates for radionuclide therapy and to subsequently perform individualised dosimetry. Consequently, it is important to understand potential limitations in the image acquisition process that will impact the accuracy and precision of quantitative estimates, and one effective method to do so is through Monte Carlo simulations.

This thesis is based on four papers utilising Monte Carlo simulations, with a focus on modelling and optimising for ^{68}Ga-PET theragnostics. Paper I explores the possibility of modelling and simulating a clinical GE Discovery MI PET system and coupling simulated data with a reconstruction software, entirely *in silico*, to enable further simulation-based studies. The implementation of correction factors emulates the processes used in clinical scanners for a more realistic approach. The model successfully generates results comparable to those obtained from a corresponding measurement on a clinical scanner. Papers II, III, and IV focus on ^{68}Ga-PET imaging of neuroendocrine tumours, with Papers III and IV also incorporating ^{177}Lu-SPECT imaging. Anthropomorphic phantoms were utilised to enable the simulation of [^{68}Ga]Ga-DOTA-TOC PET and [^{177}Lu]Lu-DOTA-TATE SPECT exams with patient-like geometries and activity distributions. In Paper II, it was shown that a non-linearly scaled administered activity based on patient weight harmonises image quality, regardless of patient body size. A harmonised image quality is important to ensure that all patients receive an equal standard of care. Paper III investigated the potential impact of respiration on quantitative estimates in [^{68}Ga]Ga-DOTA-TOC PET and [^{177}Lu]Lu-DOTA-TATE SPECT imaging. The extent of lesion motion substantially influenced the recovered lesion activity concentration, with deviations exceeding 30% from the simulated activity concentration. Furthermore, differences in quantitative bias were observed between PET and SPECT imaging, primarily attributed to the different imaging time points. In Paper IV, efforts were undertaken to elevate the realism of simulated patient models, enabling the creation of highly realistic simulated images. The ability to generate realistic images holds great future potential, as it allows for the construction of databases of simulated reconstructed

images with known ground truth. These databases can serve various purposes, including software performance evaluation and integration with machine learning. In conclusion, the use of a computational pipeline that connects Monte Carlo simulations with a reconstruction software enables simulation-based studies of entire PET-exam procedures to be conducted. Access to the underlying data driving the simulations makes it possible to isolate individual parameters and track their impact on the results, allowing for a systematic evaluation of *in vivo* confounders entirely *in silico*.

Populärvetenskaplig sammanfattning

Nuklearmedicin är en medicinsk inriktning där radioaktiva läkemedel används för att diagnosticera eller behandla olika sjukdomar. Dessa radioaktiva läkemedel består vanligtvis av två komponenter: en radionuklid[1] och själva läkemedlet. Syftet med läkemedlet är att fördela sig i kroppen utefter patientens hälsotillstånd. Radionuklider avger olika typer av strålning då de sönderfaller, och deras användbarhet inom diagnostik och terapi varierar beroende på typen av strålning de avger, främst i form av fotoner och laddade partiklar. En viktig skillnad mellan dem är att fotoner har förmågan att färdas längre sträckor och kan således lämna patients kropp, medan laddade partiklar, såsom elektroner och alfapartiklar, har en betydligt kortare räckvidd och avger sin energi lokalt för att orsaka biologisk skada.

Inom den diagnostiska grenen kan det radioaktiva läkemedlet spåras genom att detektera fotoner från det radioaktiva sönderfallet med hjälp av specialdesignade kameror. Genom att återskapa fördelningen av det radioaktiva läkemedlets upptag i kroppen kan man få en uppfattning om huruvida patientens hälsotillstånd avviker från normal fysiologisk funktionalitet. Den terapeutiska delen använder samma principer för att låta det radioaktiva läkemedlet fördela sig inom patienten, men med avsikt att orsaka biologisk skada. Vissa radioaktiva läkemedel har egenskaper som är lämpliga både för att ta bilder och behandla sjukdomen, eftersom de emitterar både fotoner och laddade partiklar.

Positron emission tomography (PET) och single photon emission computed tomography (SPECT) är två kameror som frekvent används för diagnostik inom nuklearmedicin. Den huvudsakliga skillnaden mellan PET och SPECT är dess detektionsprincip, vilket i sin tur begränsar vilka radioaktiva läkemedel som kan användas med respektive kamera. Tyvärr är kamerorna inte perfekta, och avbildningen av det radioaktiva läkemedlet tenderar att vara suboptimal.

För att förstå, förbättra och optimera prestandan hos nuklearmedicinska kameror och undersökningar kan man använda sig av Monte Carlo simuleringar. Monte Carlo metoden är en teknik som baseras på slumpmässiga urval för att uppskatta lösningar eller utfall av komplexa system, såsom strålningens interaktion och transport. Inom nuklearmedicinsk bildtagning kan Monte Carlo simuleringar användas för att skapa virtuella kamerasystem och studera undersökningsprocessen under olika förutsättningar. Monte Carlo simuleringar spelar en viktig roll inom den nuklearmedicinska forskningen genom att möjliggöra virtuella undersökningar av faktorer som är svåra att separerar i en klinisk undersökning. Genom simuleringar kan man således arbeta mot en förbättrad och optimerad undersökning, eftersom man har komplett kontroll över de parametrar man vill studera och den underliggande data som ger upphov till resultaten finns tillgänglig från

[1] En radionuklid är en instabil atomkärna som med tiden genomgår ett radioaktivt sönderfall.

simuleringarna. Dessa möjligheter finns inte i kliniska undersökningar där komplexa system interagerar med varandra och avsaknaden av den underliggande data försvårar möjligheten att reda ut orsakssamband för en parameter. Således kan Monte Carlo simuleringar användas för att på ett systematiskt sätt utforska olika faktorer som påverkar bland annat bildkvalitet och kvantifiering.

En typ av sjukdom som berörs av både diagnostisk och terapeutisk nuklearmedicin är neuroendokrina tumörer. I detta sammanhang används ett ^{68}Ga-märkt läkemedel under en PET undersökning för att fastställa sjukdomens omfattning. Beroende på utfallet så kan behandlingen sedan genomföras med ett liknande ^{177}Lu-märkt läkemedel. Effekten av behandling kan sedan följas genom SPECT-bildtagning av ^{177}Lu-läkemedlet. Användningen av liknande läkemedel för både diagnos och behandling kallas teragnostik[2] och erbjuder en unik möjlighet att skräddarsy behandlingen för varje individ.

Dock med teragnostiken kommer många utmaningar som behöver lösas. Hur kan vi säkerställa att bilderna är av tillräcklig kvalitet för en högkvalitativ diagnos? Hur kan vi öka precisionen i våra mätningar? Hur bäst identifierar vi de patienter som är lämpliga för radionuklidterapi? Hur minska vi stråldosen till friska organ samtidigt som vi maximalt strålar tumörer? Dessa är komplexa frågor att besvara, men Monte Carlo simuleringar kan vara en hjälpsam del av lösningen.

[2] Teragnostik är en sammansättning av orden terapi och diagnostik.

List of Papers

This thesis is based on the following work, distinguished by their roman numerals.

Paper I

Kalaitzidis P, Gustafsson J, Hindorf C, Ljungberg M. Validation of a computational chain from PET Monte Carlo simulations to reconstructed images. Heliyon, 2022;8(4). doi: 10.1016/j.heliyon.2022.e09316

Paper II

Kalaitzidis P, Gustafsson J, Hindorf C, Ljungberg M. Monte Carlo investigation of PET [^{68}Ga]Ga-DOTA-TOC activity-administration protocols for consistent image quality. Heliyon, 2023;9(9). doi: 10.1016/j.heliyon.2023.e19504

Paper III

Kalaitzidis P, Gustafsson J, Hindorf C, Ljungberg M. Monte Carlo investigation of respiration during [^{68}Ga]Ga-DOTA-TOC PET and [^{177}Lu]Lu-DOTA-TATE SPECT imaging. Manuscript submitted to Phys Med Biol, (2023).

Paper IV

Kalaitzidis P, Curkic Kapidzic S, Sjögreen Gleisner K, Hindorf C, Ljungberg M, Gustafsson J. Improved patient models for simulation of clinically realistic ^{68}Ga-SSTR PET and ^{177}Lu-PRRT SPECT studies. Manuscript, (2023).

Author's contribution to the papers

The work in this thesis follows a logical order in which implementations from one simulation are applied in the next. In Paper I, the construction of the pipeline connecting simulated data to reconstructed images is carried out and validated. In Paper II, applications within [^{68}Ga]Ga-DOTA-TOC for optimising image quality are conducted using patient-like models with the pipeline from paper I. In Paper III, the results from Paper II are applied, and the investigation is extended to evaluate the impact of respiration on quantitation for the theragnostic pair [^{68}Ga]Ga-DOTA-TOC PET and [^{177}Lu]Lu-DOTA-TATE SPECT through simulations. In Paper IV, efforts were made to enhance the realism of the patient model with a primary focus on applications for the theragnostic pair [^{68}Ga]Ga-DOTA-TOC and [^{177}Lu]Lu-DOTA-TATE.

Paper I: **Validation of a computational chain from PET Monte Carlo simulations to reconstructed images**

Contributions: I developed the PET Monte Carlo model, constructed the programs necessary for computing correction factors for quantitative PET, and wrote the program finalising the connection to reconstructed images. Additionally, I participated in the phantom measurements and performed the simulations and the following reconstructions. I analysed and interpreted the data, and I authored the manuscript, serving as the corresponding author.

Paper II: **Monte Carlo investigation of PET [^{68}Ga]Ga-DOTA-TOC activity-administration protocols for consistent image quality**

Contributions: I constructed the patient model and defined the simulated radiopharmaceutical distribution to mimic a [^{68}Ga]Ga-DOTA-TOC PET exam. I performed the simulations and reconstructions. I analysed and interpreted the data, and I authored the manuscript, serving as the corresponding author.

Paper III: **Monte Carlo investigation of respiration during [^{68}Ga]Ga-DOTA-TOC PET and [^{177}Lu]Lu-DOTA-TATE SPECT imaging**

Contributions: I constructed the patient model with respiratory motion. I performed the PET simulations and reconstructed the PET images. I analysed and interpreted the data, and I authored the manuscript, serving as the corresponding author.

Paper IV: **Improved patient models for simulation of clinically realistic ^{68}Ga-SSTR PET and ^{177}Lu-PRRT SPECT studies**

Contributions: I implemented improvements to enhance the realism of the patient model. These improvements, in addition to the use of anthropomorphic phantoms and the inclusion of respiratory motion (added in **Paper II** and **Paper III**, respectively), included the incorporation of heterogeneous tumour activity, non-

uniform normal-organ activity concentration, and the use of realistic patient tumours. I conducted the PET simulations and carried out the PET reconstructions. I participated in part of interpreting and analysing the data. I was one of the main authors of the paper.

Abbreviations

BGO	Bismuth germanium oxide
BSREM	Block-sequential regularised expectation-maximisation
CASToR	Customizable Advanced Software for Tomographic Reconstruction
CSDA	Continuous slowing down approximation
CT	Computed tomography
CZT	Cadmium zinc telluride
EM	Expectation-maximisation
FBP	Filtered back-projection
FOV	Field of view
FWHM	Full width at half maximum
GATE	Geant4 Application for Tomographic Emission
LOR	Line of response
LSO	Lutetium oxyorthosilicate
LYSO	Lutetium yttrium oxyorthosilicate
MC	Monte Carlo
ML-EM	Maximum-likelihood expectation-maximisation
MRI	Magnetic resonance imaging
NEC	Neuroendocrine carcinoma
NEN	Neuroendocrine neoplasm
NET	Neuroendocrine tumour
NURBS	Non-uniform rational B-splines
OS-EM	Ordered-subset expectation-maximisation
PET	Positron emission tomography
PMT	Photomultiplier tube
RC	Recovery coefficient
PDF	Probability density function
PRRT	Peptide receptor radionuclide therapy
PVE	Partial volume effect

SiPM	Silicon photomultiplier
SPECT	Single photon emission computed tomography
SSS	Single scatter simulation
SSTR	Somatostatin receptor
TOF	Time of flight

1. Introduction and Aims

Nuclear medicine imaging

Nuclear medicine imaging non-invasively generates functional information for diagnostic purposes. A radioactive molecular agent (radiopharmaceutical) is administered to the patient, which is then distributed within the patient's body based on the patient's physiology and the agent's physiological mechanisms. Imaging typically occurs after some time to allow the radiopharmaceutical to distribute within the patient's body. Information regarding the radiopharmaceutical distribution is used to evaluate the patient's current physiological functionality through various intermediate indicators, including but not limited to tissue blood flow, metabolism, and cell receptor expression. Deviations from typical physiological patterns are an indication of pathological functionality.

The radiopharmaceutical is detected and reconstructed into volumetric images through gamma camera imaging or positron emission tomography (PET). The gamma camera detects photons and relies on a physical collimator to determine lines along which the emitted photons originated from. PET, on the other hand, requires the detection of two annihilation photons in coincidence, and the lines along which the annihilations occurred are determined through electronic collimation.

The choice of the molecular agent is determined by the physiological mechanism to be studied, while radionuclide selection is based on chemical compatibility with the molecular agent. A prerequisite is that the introduction of the radionuclide does not change the physiochemical characteristics of the molecular agent, as even minor changes will alter its *in vivo* physiological behaviour (Fani et al. 2011, Fani et al. 2012). This obviously limits the number of radiopharmaceuticals that are available to study a specific physiological property. The choice between gamma camera imaging or a PET thus primarily depends on the availability of radiopharmaceuticals for studying the desired physiological mechanism.

Theragnostics and Monte Carlo simulations

One application that has gained increasing popularity in recent years is theragnostics (Herrmann et al. 2020). In nuclear medicine, theragnostics involves using molecular agents of similar physiological targeting mechanisms for diagnosis and therapy, allowing the visualisation of therapeutic targets before administering the therapeutic

agent. This distinctive capability can be utilised in several clinical applications, including the visual assessment of the biodistribution of targeted drugs, visualisation of tumour burden, and the selection of patients for targeted therapies, enabling a *'treat-what-you-see'* strategy (Bodei et al. 2022). Repeat peri-therapeutic imaging enables dosimetric calculations which can further facilitate treatment optimisation by finding a balance between efficacy and toxicity (Sundlöv and Sjögreen Gleisner 2021).

Theragnostics thus holds the potential to generate individualised treatment strategies to improve therapy outcomes through pre-therapeutic and peri-therapeutic image-based quantification. However, to fully appreciate the significance of these metrics, it is imperative to understand the complexities of image degradation and the risk for biased estimates. Dedicated efforts to deepen our understanding of these factors are therefore important to the advancement of the field.

However, disentangling these factors can be challenging in a clinical setting due to the complexity and interplay between anatomy, physiology, fundamental physics, and imaging instrumentation, which all complicate the assessment of a single parameter's impact. When combined with computational human phantoms, Monte Carlo (MC) simulations, which is a probabilistic numerical technique that can be used to solve non-deterministic problems, enable realistic modelling of patient measurements and to systematically evaluate individual parameter's impact on the resulting image. Hence, the combination of MC simulations and anthropomorphic patient models provides a good compromise between the need for controlled experiments and patient-like geometry, which can help to enhance our understanding of parameters that are challenging to separate in clinical settings.

Aims

The aim of this thesis was to work with ^{68}Ga-PET, with a primary focus on modelling and optimisation, towards theragnostic applications.

A pipeline connecting PET simulations to reconstructed images for [^{68}Ga]Ga-DOTA-TOC applications was constructed. Methods have also been introduced to enhance the realism of simulations, so that these better correspond to that of a patient undergoing a clinical exam. Additionally, the integration of [^{177}Lu]Lu-DOTA-TATE simulations enables simulation-based studies tailored to theragnostics applications.

Specifically, the aims of **Papers I–IV** were:

I. To create and validate a pipeline connecting PET Monte Carlo simulations to reconstructed images. The connection from simulation to reconstructed images is highly important as it provides possibilities to emulate the entire PET exam chain, and, most importantly, the ability

to evaluate the end product, i.e., the reconstructed image. The validation enables the pipeline's use in future simulation-based studies and ensures the reliability of the results.

II. To evaluate various [^{68}Ga]Ga-DOTA-TOC activity-administration protocols ability to achieve a harmonised image quality based on patient habitus. Harmonised image quality promotes an equal standard of care, irrespective of patient body size.

III. To investigate the impact of respiratory motion on quantitative [^{68}Ga]Ga-DOTA-TOC PET and [^{177}Lu]Lu-DOTA-TATE single photon emission computed tomography (SPECT). Understanding how respiration affects quantitative accuracy is important if image-based metrics are to be used in individual treatment stratification for the theragnostic pair.

IV. To propose a methodology for enhancing the realism of patient models for [^{68}Ga]Ga-DOTA-TOC PET and [^{177}Lu]Lu-DOTA-TATE SPECT Monte Carlo simulations. This method can generate databases of images more visually comparable to clinical images, which is relevant for tasks such as software performance assessment or machine learning.

2. Nuclear Medicine Imaging

Positron Emission Tomography

Positron emission tomography aims to reveal a patient's current physiological status by mapping the distribution of an administered positron-emitting radiopharmaceutical. The radiopharmaceutical is mapped by detecting the subsequent photon emission following positron-electron annihilation.

After a positron is emitted through a radioactive decay, it gradually decelerates until it comes to rest. Subsequently, an interaction with an atomic electron results in the annihilation of the two particles. In this annihilation process, the positron and electron are converted into two opposite-directed annihilation photons, each with an energy of 511 keV, due to conservation of mass-energy and momentum. Annihilation can occur before the positron is completely at rest, leading to a slight angular deviation between the two photons.

Data formation in PET relies on detection in coincidence, and this detection is made possible by opposing scintillator-based detectors often arranged in a circular configuration. Common scintillator materials include cerium-doped lutetium-based crystals (LSO:Ce/LYSO:Ce) or bismuth germanium oxide (BGO).

A coincidence window is triggered when an annihilation photon impinges on a detector and deposits its energy, and a coincident event will be registered if two coincidence windows are opened simultaneously by different detectors. In practice, simultaneous detection implies the detection of two annihilation photons within a predefined time window.

The detection of a coincident event indicates the occurrence of a positron-electron annihilation at some point along a fictitious line called a line of response (LOR) that spans between the two registering detectors. If the difference in detection time could be measured precisely enough, the exact position along the LOR could be determined, potentially eliminating the need for tomographic reconstruction (Lecoq et al. 2020).

However, the annihilation's position can only be narrowed down within a few centimetres along the LOR due to the detectors finite temporal resolution, which then still necessitates tomographic reconstruction (Surti 2015). Nevertheless, the introduction of time of flight (TOF), i.e., measuring the time difference between the

two detections, leads to improved noise characteristics in the reconstructed image (Budinger 1983, Lois et al. 2010).

The collection of all coincident events is called prompt coincidences and includes true, scattered, and random coincidences. Random and scattered coincidences will misplace the LOR in relation to the annihilation site. Scattered coincidences arise when at least one of the annihilation photons undergoes incoherent scattering before detection, resulting in the emission of new a photon with decreased energy and deflected by an angle relative to the incident photon. Scattered coincidences have a relatively low-frequency distribution around the annihilation site. Random coincidences, on the other hand, occur when two uncorrelated photons are detected within the coincidence timing window. Thus, random coincidences only shares an indirect relation with the radiopharmaceutical distribution, resulting in a relatively uniform background. Figure 2.1 illustrates true, random, and scattered coincidences.

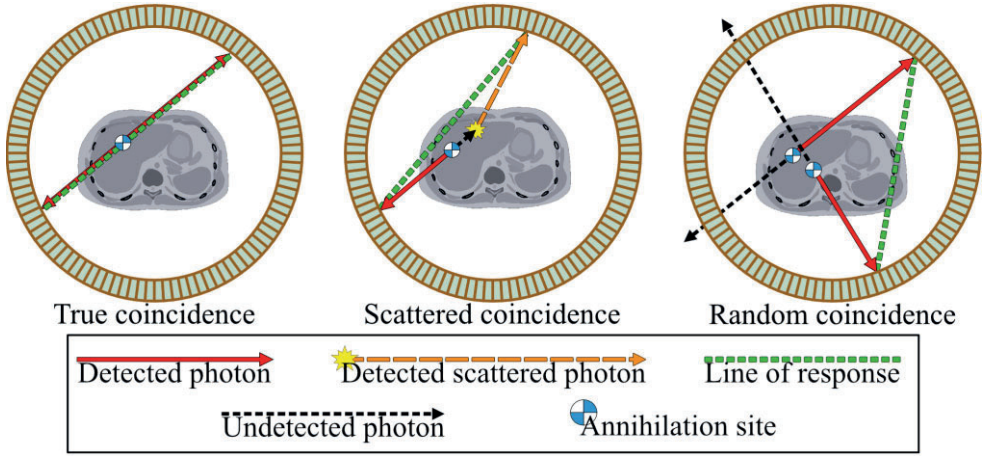

Figure 2.1: True, scattered, and random coincidences and how the LOR is misplaced depend on the coincidence type is shown. The distribution of random coincidences is uncorrelated with the site of annihilation, while scattered coincidences share some relation to the site of annihilation.

The presence of mispositioned LORs degrades image quality and hampers accurate quantitative estimations. As a result, electronic collimation is imposed whereby constraints are implemented in the signal-processing chain to prevent unwanted photons from forming coincidences. One part of the electronic collimation is the coincidence timing window, i.e., a predefined time window in which photons must be detected to be able to form coincidences. The coincidence window is kept as narrow as possible to reduce the number of random coincidences while at the same time ensuring that true coincidences can be detected within the scanner's field of view (FOV). The minimum width is chosen so that annihilation photons generated

at the very edge of the FOV will have sufficient time to traverse and be detected in the very opposite part of the scanner, i.e., the longest valid LOR indirectly sets the minimum coincidence window width. Energy discriminators attempts to reject scattered and high- and low-energy photons, by only allowing photons that fall within a predefined energy range around the annihilation photopeak to form coincidences. Reducing the width of the energy window increases the rejection of scattered photons. However, if set to narrow, the finite energy resolution imposed by the detector would result in a substantial number of true unscattered annihilation photons being erroneously rejected. Additionally, factors such as attenuation and non-uniform sensitivity also impact PET data formation. However, electronic collimation cannot address these factors; they are handled separately.

Lines of responses are characterised by their angle, radial distance from the scanner's centre, and axial location. These LORs collectively represent the spatial distribution of annihilation sites, and they are subsequently reconstructed into a volumetric image that depicts regional radiopharmaceutical concentration to facilitate the diagnostic interpretation process. Initially, the reconstruction provides a semi-quantitative representation of the radiopharmaceutical intensity. However, after compensating for image-degrading effects, the reconstructed images can be calibrated to provide quantitative voxel values since the number of true coincidences within the LORs is proportional to a line integral of the activity along the LORs (Meikle and Badawi 2005).

The evaluation is in many cases qualitative without the need for absolute voxel value quantification. Nonetheless, quantitation in PET is less observer-dependent and can provide added benefits in theragnostics, precision medicine, and PET biomarkers (Lammertsma 2017, Kinahan et al. 2020, Meikle et al. 2021). However, standardisation is essential as minor instrumental and physiological differences can lead to substantial differences in quantification (Boellaard 2009), and understanding the bias and its dependence on technical, physiological, and scanner settings is essential.

Modern PET scanners are combined with computed tomography (CT) or magnetic resonance imaging (MRI) to enhance diagnostic capabilities. The combined imaging provides an anatomical reference to the physiological information while also providing necessary data to perform attenuation and scatter correction.

Some common PET isotopes include ^{18}F, ^{68}Ga, ^{15}O, and ^{11}C. These isotopes have distinct characteristics that influence the logistics and quality of the PET exam, such as half-life and positron energy. Table 2.1 lists some important properties of a few common PET isotopes.

Table 2.1
Properties of some positron-emitting radionuclides and medical applications. Data acquired from the Laboratoire National Henri Becquerel database (Be et al. 2004, Be et al. 2013). Some isotopes have multiple decay transitions, e.g., ^{68}Ga, and listed is the most common transition. The positron range is shown in the continuous slowing down approximation (CSDA) in water for the listed max and mean positron energies (ICRU 1984).

Nuclide	Half-life [min]	Positron fraction [%]	E_{max} [keV]	E_{mean} [keV]	Max range [mm]	Mean range [mm]
^{11}C	20.36	99.75	960.5	385.7	4.18	1.20
^{13}N	9.97	99.82	1198.5	493.0	5.49	1.72
^{15}O	2.04	99.89	1735.0	736.7	8.48	2.97
^{18}F	109.73	96.86	633.9	249.5	2.43	0.62
^{68}Ga	67.83	87.68	1899.1	836.0	9.39	3.50

Attenuation correction

The number of registered coincidences is typically reduced due to photon interactions in which either of the two photons are absorbed within the object or scattered outside the imaging FOV. This attenuation effect is spatially dependent, with photons traversing more material having a lower likelihood of reaching a detector. Consequently, the effect of attenuation is more pronounced in large objects, which leads to a spatially variable intensity in the reconstructed image. Nevertheless, computation of attenuation correction factors for PET is straightforward (Kak and Slaney 1988).

Consider two annihilation photons heading towards the detector pair (D_1, D_2) from the annihilation point AP. The probability of each photon reaching its respective detector is given by $\exp[-\int_{AP}^{D_1} \mu_Z(x)dx]$ and $\exp[-\int_{D_2}^{AP} \mu_Z(x)dx]$, where $\mu_Z(x)$ is the linear attenuation coefficient at 511 keV. The probability of both photons reaching their detectors is determined by the product of probabilities of reaching their respective detector, i.e.,

$$\exp\left[-\int_{D_1}^{D_2} \mu_Z(x)dx\right] = \exp\left[-\int_{AP}^{D_1} \mu_Z(x)dx\right] \cdot \exp\left[-\int_{D_2}^{AP} \mu_Z(x)dx\right]. \qquad (2.1)$$

Hence, the probability of attenuation is the same for all sources independent of position along an LOR. The attenuation correction factor for an LOR is obtained by computing the reciprocal of equation (2.1), with the ray sums computed from an image of linear attenuation coefficients of the object.

Normalisation

The sensitivity of a PET scanner varies across the FOV due to differences in, e.g., detector efficiency, differing solid angle subtended by LORs, and summation of adjacent detector elements. Correcting for these variations is essential; otherwise, the non-uniform sensitivity will propagate to the reconstructed image, leading to biased quantitative estimates and unwanted artefacts. Normalisation of the data is typically performed using a component-based method (Hoffman et al. 1989, Badawi and Marsden 1999), which estimates the impact of individual factors contributing to the sensitivity variation in each unique LOR.

In a block-detector system, a systematic efficiency variation occurs due to the crystal's position in the block, resulting in significant sensitivity fluctuations. The sampling of LORs tightens near the edges of the FOV, leading to a reduced acceptance angle and, consequently, reduced sensitivity. However, this effect is partially mitigated transaxially since the detectors are closer together, as illustrated in Figure 2.2. Furthermore, a photon entering a crystal at an angle typically has more material to traverse than a photon entering normally. This increases the probability of detection and results in measurable sensitivity changes based on the LOR's radial position. Notwithstanding, a photon entering a detector block near its edge and at an angle usually has less material to traverse, which increases the likelihood that the photon escapes the crystal before interacting. This leads to a sensitivity pattern that varies with both the LOR's radial position and the crystal's location within the block. Other factors affecting the non-uniformity, such as accurate detector alignment, time window alignment (i.e., synchronicity between timing signals), and variations in crystal composition are not included within the context of this thesis as they are not expected to be present in the Monte Carlo simulations.

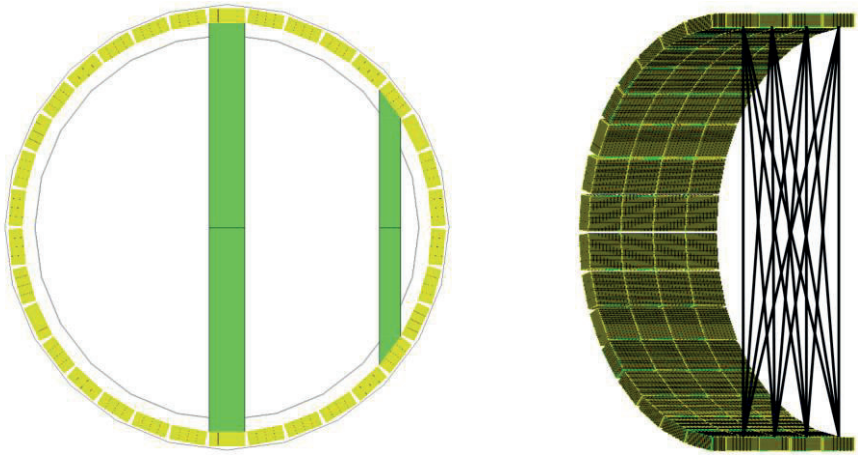

Figure 2.2: The acceptance angle decreases at the edge of the FOV, both transaxially and axially, leading to a reduced sensitivity. However, the sensitivity increases as the detectors are positioned closer together in the transaxial plane.

The normalisation factors computed within the context of this thesis include the intrinsic detector efficiency (ε) and the axial block profile factor (b) to account for systematic sensitivity variations due to the crystal's transaxial and axial position in the scanner. The axial geometric factor (g) and the radial profile factor (r) are incorporated to account for the axial and transaxial variations in LOR efficiency related to the photon's angle of incidence on the crystal face, respectively, and lastly, the crystal interference factor (f) is considered to account for changes in the radial profile factors due to the crystal's relative position within the block. Hence, the normalisation coefficient for an LOR spanned by two detectors, D_1 and D_2, is computed as

$$\eta_{D_1D_2} = \varepsilon_{D_1}\varepsilon_{D_2} b^{\mathrm{ax}}_{D_1} b^{\mathrm{ax}}_{D_2} g^{\mathrm{ax}}_{D_1D_2} r^{\mathrm{tr}}_{D_1D_2} f^{\mathrm{tr}}_{\varphi\%D}. \tag{2.2}$$

The individual normalisation components are shown in Figure 2.3. Figure 2.4 shows the impact of omitting individual transaxial normalisation factors on the reconstructed image.

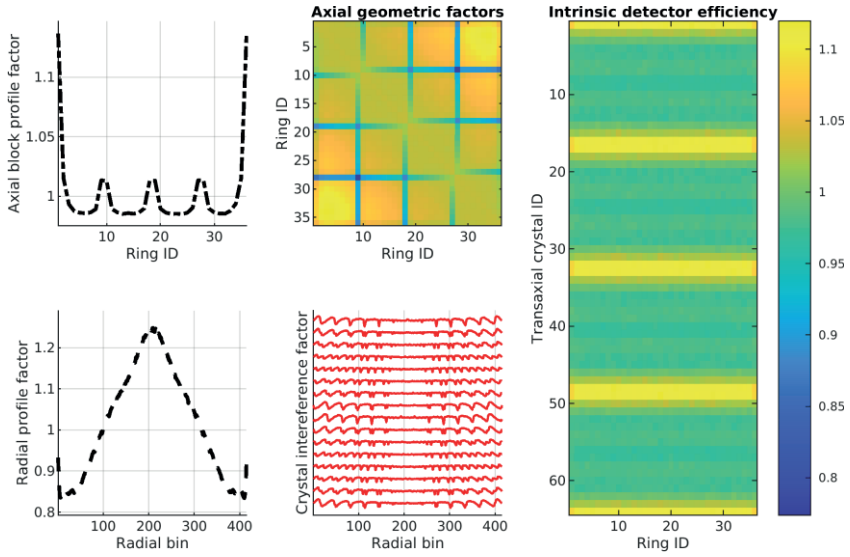

Figure 2.3: The individual normalisation factors used in equation (2.2) are presented. The crystal interference factors are offset from each other to demonstrate sensitivity variations based on the LOR's radial position and the crystal's transaxial position within a block. The intrinsic detector efficiency factors are shown for the first 65 transaxial crystals and exhibit a clear systemic variation in sensitivity.

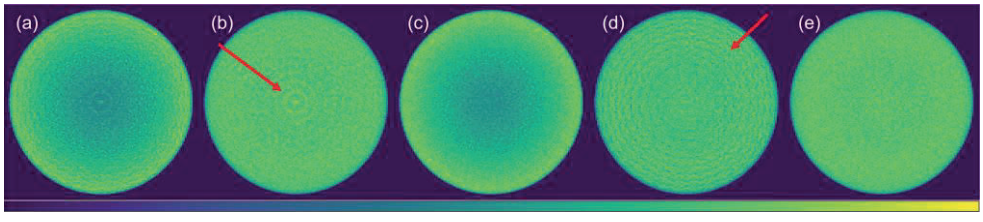

Figure 2.4: Reconstructed images of a source covering the entire transaxial FOV: without any normalisation (a); without compensation for intrinsic detector efficiency (b); without compensation for the radial profile factors (c); without compensation for the crystal interference factors (d); and fully normalised (e). High-frequency artefacts appear as the intrinsic detector efficiency factor is not compensated for (b); a pronounced intensity drop occurs radially inwards as the radial profile factor is omitted (c); and without compensation for the crystal interference the appearance of ringing artefacts occurs (d).

Randoms correction

The finite width of the coincidence window introduces the risk of detecting two uncorrelated photons closely in time, resulting in the formation of random coincidences as the electronic collimation cannot distinguish them from true unscattered annihilation photons. Random coincidences lack spatial information and

result in a fairly uniform distribution across the FOV (Hoffman et al. 1981), reducing image contrast and leading to inaccurate activity concentration estimation.

The rate by which random coincidences are formed depends on the singles count rate onto each detector and the width of the coincidence window. A coincidence timing window with a duration of τ is opened when a photon is detected. Another coincidence window is opened if another photon is detected, and a coincidence is registered if the two coincidence windows overlap. Therefore, the time during which a coincidence can be recorded is 2τ. Assuming that the photons are uncorrelated, the rate of detecting random coincidences will be

$$R_{D_1 D_2} = 2\tau r_1 r_2, \tag{2.3}$$

where r_1 and r_2 are the singles rate onto detectors D_1 and D_2, respectively.

Scatter correction

There is a risk that one or both of the annihilation photons will interact with the imaged object before detection, and the most common interaction at the energy of annihilation photons is Compton scattering. Due to scintillation detectors' inherent energy resolution limitations, some scattered photons cannot be distinguished from unscattered ones. Consequently, if a coincidence is registered after one or both annihilation photons have scattered, the coincidence will no longer be colinear with the annihilation site. Scattered coincidences account for a substantial fraction of the recorded coincidences (Cherry and Huang 1995) and depend on the size and composition of the imaged object and the PET scanner configuration and settings. Scattered coincidence leads to a loss of image contrast and inaccuracies in activity concentration estimation.

Scatter correction in PET is typically handled using a model-based approach (Ollinger 1996) and a common implementation is the single scatter simulation (SSS) algorithm (Watson 1996). This algorithm exploits the characteristics of the scattering phenomenon to approximate its distribution and intensity, and the fundamental concept behind the SSS algorithm is to estimate the scattered coincidences based on potential scatter points within the imaged object.

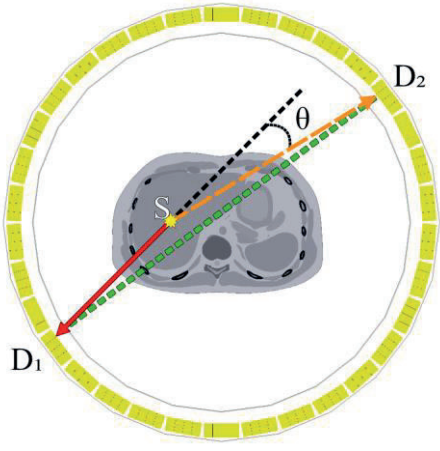

Figure 2.5: The geometry of the scatter model is presented in a two-dimensional representation, but the underlying concept operates within a three-dimensional framework. The LOR (green dashed line) is no longer colinear with the annhilation site after one of the annihilation photons scatters at *S* by an angle *θ*.

The scatter contribution to an LOR, spanned by the detectors D_1 and D_2, from a scatter point S, can be estimated by considering (based on the geometrical representation in Figure 2.5):

1. The attenuation along SD_1 for the unscattered photon.
2. The integrated source intensity along SD_1.
3. The probability of scattering at S towards D_2.
4. The attenuation along SD_2 for the scattered photon.
5. The detection efficiency of the scattered and unscattered photon.

The events that resulted in a scattered coincidence could have occurred with the scattered and unscattered rays reversed. Hence, the scatter coincidence rate for an $\mathrm{LOR}_{D_1D_2}$ is calculated as $R_{\mathrm{sct},S}^{D_1D_2} = R_{\mathrm{sct},S}^{D_1} + R_{\mathrm{sct},S}^{D_2}$, where $R_{\mathrm{sct},S}^{D_1}$ is calculated as

$$R_{\mathrm{sct},S}^{D_1} = \int_S^{D_1} \lambda(s)\, ds \cdot \exp\left(-\int_S^{D_1} \mu_Z(E,s)ds\right) \cdot \exp\left(-\int_S^{D_2} \mu_Z(E_{\mathrm{sct}},s)ds\right) \cdot \varepsilon(E)_{SD_1} \cdot \varepsilon(E_{\mathrm{sct}})_{SD_2} \cdot \frac{\sigma_{SD_1}\sigma_{SD_2}}{4\pi l_{SD_1}^2 l_{SD_2}^2} \frac{\mu_Z}{\sigma_c} \frac{d\sigma_c(\theta)}{d\Omega}, \tag{2.4}$$

and $R_{\mathrm{sct},S}^{D_2}$ as

$$R_{\mathrm{sct},S}^{D_2} = \int_S^{D_2} \lambda(s)\, ds \cdot \exp\left(-\int_S^{D_2} \mu_Z(E,s) ds \right) \cdot \exp\left(-\int_S^{D_1} \mu_Z(E_{\mathrm{sct}},s) ds \right) \cdot$$
$$\varepsilon(E_{\mathrm{sct}})_{SD_1} \cdot \varepsilon(E)_{SD_2} \cdot \frac{\sigma_{SD_1}\sigma_{SD_2}}{4\pi l_{SD_1}^2 l_{SD_2}^2} \frac{\mu_Z}{\sigma_c} \frac{d\sigma_c(\theta)}{d\Omega}, \quad (2.5)$$

where λ is the source intensity, μ_Z is the linear attenuation coefficient, E and E_{sct} represent the unscattered and scattered photon energy, respectively, ε is the detector efficiency, σ_{SD_1} and σ_{SD_2} are the detector geometric cross-sections, l is the distance from the scatter point to the detector, σ_c and $d\sigma_c(\theta)/d\Omega$ are the total and differential Compton interaction cross-sections. Equation (2.4) accounts for emissions contributing to the scattered coincidences originating from the SD_1 side of S, while equation (2.5) accounts for the contributions originating from the SD_2 side of S. The ray sums in equations (2.4) and (2.5) are computed by ray tracing through images of the source distribution and the object's linear attenuation coefficients.

Scattered coincidences have a temporally varying distribution, which requires additional considerations when estimating the TOF scatter contribution. The contributions of a scattered coincidence to a specific TOF bin depend on both the position of the emission point and the length difference of the rays forming one scatter path. Consequently, there is a unique detection probability that depends on the detectors' temporal resolution (or associated distance), τ_{res}, and the spatial offset from the scatter point, Δs, that the scattered coincidence will be recorded in the t^{th} TOF bin (Watson 2007). This TOF detection probability is typically modelled by sampling a Gaussian as

$$\varepsilon_t(\Delta s) = \frac{e^{-\frac{(\Delta s - t\tau_{\mathrm{res}})^2}{2\sigma^2}}}{\sum_{t'} e^{-\frac{(\Delta s - t'\tau_{\mathrm{res}})^2}{2\sigma^2}}}, \quad (2.6)$$

where σ is the standard deviation. Equation (2.6) is then incorporated into the source ray sums in equations (2.4–2.5) to estimate the TOF scatter contribution. The total scatter contribution can then be estimated by evaluating the additive contributions from all potential scatter points, i.e.,

$$R_{\mathrm{sct,tot}}^{D_1 D_2} = \sum_S R_{\mathrm{sct},S}^{D_1 D_2}. \quad (2.7)$$

The ray sums in equations (2.4–2.5) are computed from an initial source and attenuation image. The source image can be reconstructed in various ways but must be corrected for attenuation, normalisation, and randoms, and a fast way to do this is to reconstruct using the filtered back-projection method. However, as equation (2.7) is sampled for every potential scatter point and ray sums are computed for

every detector-pair permutation, the computation becomes very time-consuming, and for a system like the GE Discovery MI, comprised of 19584 scintillation crystals, utilising the SSS algorithm for scatter estimation becomes impractical. Therefore, the detector system, source image, and attenuation image are down-sampled to a sparsely defined scanner and to coarsely gridded images to accelerate the computation. Although down-sampling reduces the image spatial resolution, the effect is not detrimental to the scatter estimation, as scattered coincidences primarily exhibit a low-frequency distribution (Werling et al. 2002).

After the scatter estimate has been evaluated for all potential scatter points, the sinogram is up-sampled and interpolated to match the original sinogram's dimensions. The estimated scatter is then scaled as a linear transformation, with the scaling parameters determined from a linear least-squares fit of the estimated scatter to the randoms-subtracted measured data. Scatter estimations involving radionuclides with prompt gamma emission are typically accounted for during the scaling process (Surti et al. 2009). However, careful consideration must be taken to ensure that only bins situated outside the object volume are used, as the inclusion of any true coincidences would impact the scaling process (Thielemans et al. 2007).

The SSS algorithm is performed iteratively to successively improve the scatter estimate. The scatter estimate will be overestimated in the first iteration as the initial reconstruction contains both true and scattered coincidences. In the subsequent iteration, the overestimated scatter estimate leads to an underestimated reconstructed image, resulting in an underestimation of scattered coincidences. After two iterations, the scatter estimate is averaged between the first and second iterations to expedite the convergence and to reduce the risk of excessive oscillation between successive scatter estimations (Iatrou et al. 2006). Figure 2.6 shows an example of the scatter estimation process for the first three iterations.

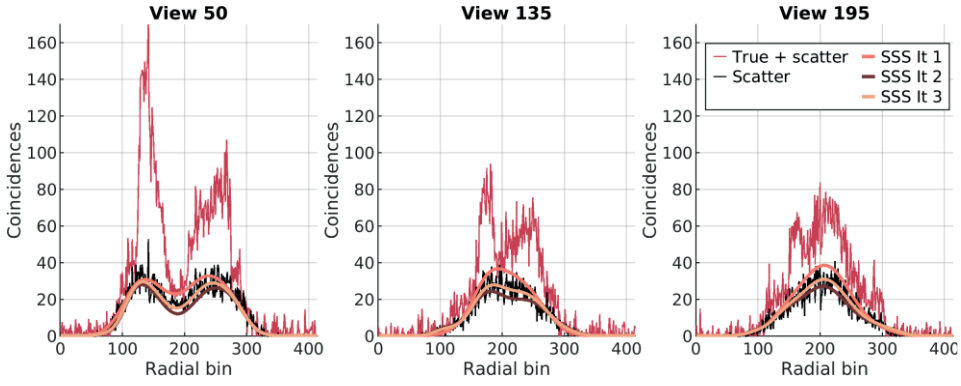

Figure 2.6: An example of SSS estimated scatter following a PET MC simulation. The MC simulated meta data is used to show the exact number of scattered coincidences. A total of three SSS iterations are shown for three different projection views. The estimated scatter is progressively improved as the number of iterations increases.

Deadtime

Deadtime refers to the period when the system is busy processing a previously detected event, during which the system does not properly record new events. Deadtime constitutes two primary mechanisms: 1) due to a finite resolving time, some counts will be ignored entirely, and 2) multiple photons can arrive sufficiently close in time at high count rates, whereby they will be processed together (pile-up). Pile-up results in two distinct effects: the summation of multiple photon energies can result in losses of unscattered photons if the summed energy falls outside of the energy discriminators, or the event will be registered but mispositioned in systems employing multiplexing (Germano and Hoffman 1990). Consequently, high count rates may affect the system's uniformity and linearity.

In practice, deadtime losses are dominated by pile-up within the crystal. Cameras with a larger number of discrete scintillation detectors can often operate at higher count rates before being affected by pile-up compared to systems employing a higher degree of multiplexing.

Calibration

Once the corrections have been computed, the reconstructed image can be calibrated to yield absolute units of activity concentration. The calibration is typically performed by imaging with a phantom with a known activity that has been measured within a well counter prior to imaging. After acquisition, the image is reconstructed and the aforementioned image-degrading components are compensated for. The image voxel values are then directly compared with the activity concentration determined by the well counter to compute a calibration factor. This is a fast and straightforward method for determining a calibration factor.

However, it is important to note that this procedure may not necessarily produce an accurate calibration factor if the well-counter results are biased. In the case of the Monte Carlo simulations described herein, the calibration was performed using this method, and since the exact activity concentration is known, any bias from a well counter will not propagate to the calibration factor.

The Gamma Camera

The primary components of a common type of gamma camera consist of a scintillation crystal with photomultiplier tubes (PMTs) attached to the back face of the crystal, encased within a shield casing. A fundamental requirement of the gamma camera is to determine the position and energy of interacting photons. Typically, the relative signals shared by the PMTs, weighted by their position, are used to determine the photon's interaction point. However, due to the isotropic photon emission, the position of the photon interaction within the camera alone conveys no spatial information about the emission. A physical collimator is therefore used to restrict the detection of photons to only those directionally parallel with the collimator's holes. Several types of collimators exist designed for specific purposes, but the most widely used and the one discussed henceforth, is the parallel-hole collimator. With the parallel-hole collimator design, only photons that are normally incident (within a small acceptance angle) towards the scintillator crystal will be allowed to pass the collimator to be detected. For the detection to be registered as a count, the deposited energy from the interaction must fall within a predefined energy range, which is selected based on the photon's energy and the scanner's energy resolution. Similar to PET imaging, the acquisition process is imperfect and effects of, e.g., attenuation and scatter will impact the acquisition and must be compensated for. An illustration of the gamma camera and a few typical events are shown in Figure 2.7.

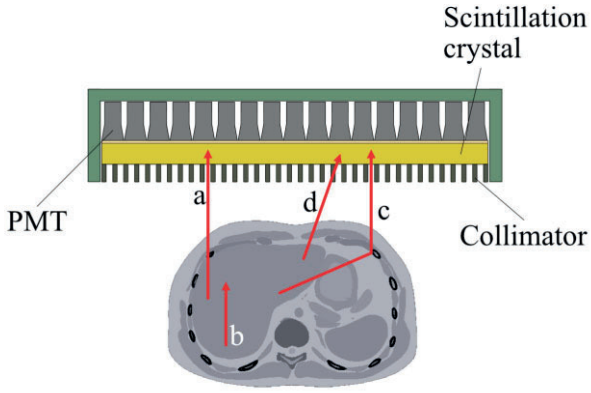

Figure 2.7: Illustration of the gamma camera and a few typical events. A photon parallel with the collimator holes can pass the collimator and interact with the crystal (a). The photon is attenuated in the object (b). The photon is scattered in the object, which may lead to the subsequent alignment with the holes by which the photon can be detected (c). The photon is not stopped by the collimator and can still be detected (d).

The projections acquired with a parallel-hole collimator will convey information about the radiopharmaceutical's distribution summed over the object's depth. Consequently, the acquired projections carry no depth information as photons can be detected at the same position in the camera but originate from different depths. By rotating the gamma camera about the object, projections can be acquired from multiple angles, akin to a PET acquisition, by which the three-dimensional distribution of the radiopharmaceutical can be recovered.

System Characteristics

Spatial resolution

Spatial resolution refers to the spatial limit for which a system can represent objects and is defined by the smallest distance needed for adjacent point sources to be distinguished as distinct entities.

The fundamental PET spatial resolution is dependent on the physics of positron interactions and the scanner configuration. Positrons are typically ejected with non-zero energy and interacts and travels a distance before losing its kinetic energy, which results in annihilations occurring away from the radionuclide's decay site, leading to a blurring of the PET image. The extent of blurring depends on the kinetic energy of the positron and the composition of the material traversed (Sanchez-Crespo 2013). Table 2.1 lists common isotopes used in PET imaging and positron

range in water of the associated ejected positron. Additionally, the annihilation can occur before the positron has come to rest. In such cases, the annihilation photons will no longer be colinear, with a mean accollinearity angle of 0.25° full width at half maximum (FWHM) (Colombino et al. 1965). The magnitude of this effect depends on the scanner's geometry, and a wider detector ring radius, R, exacerbates its impact. The blurring associated with photon acollinearity, in terms of distance, is given by $0.0044R$ (Moses 2011).

The detector size also influences the spatial resolution, and its impact can be assessed by examining the coincidence detection sensitivity between a pair of opposing detectors. Near the midpoint between the two detectors, the coincidence rate is characterised by a triangular response function with an FWHM equal to half the detector width (Levin and Hoffman 1999). However, the response function is better characterised by a trapezoidal function as the source is moved closer to either of the two detectors, i.e., the spatial resolution worsens further from the scanner's centre. Photons also typically penetrate the scintillation crystal some distance before interacting. The photon may thus be detected by a different crystal if the photon is not normally incident on the crystal, which results in the LOR being assigned to the wrong crystal. This blurring is asymmetric and becomes more pronounced with increasing radial distance from the scanner's centre, but its impact is less severe in scanners employing scintillator crystals with high linear attenuation coefficients (Derenzo et al. 1981). However, the effect is not considered fundamental as systems employing depth of interaction detection could alleviate its impact (de Jong et al. 2007). Additional effects related to crystal decoding and imperfect LOR sampling also degrades the spatial resolution, but their effects are not considered fundamental (Moses 2011).

The unavoidable fundamental PET spatial resolution limit for a point source is set by the positron range, photon acollinearity, and detector size (Levin and Hoffman 1999) and can be determined as

$$\Gamma = \sqrt{\left(\frac{d}{2}\right)^2 + s^2 + (0.0044R)^2}, \tag{2.8}$$

where d is the detector width, s is the blurring due to the positron range, and R is the scanner radius. In theory, one could potentially reduce the detector width indefinitely to truly reach a fundamental spatial resolution limit. Constructing detectors with an infinitely small width is however not practically feasible. At some point, the effects of positron range and accollinearity will dominate, and continuing to reduce the detector width at this juncture makes little sense.

The spatial resolution limit of a gamma camera depends primarily on technical limitations, specifically the collimator's design (Rahmim and Zaidi 2008). The configuration of a parallel-hole collimator defines the maximum acceptance angle by which photons can interact with the crystal if no septal penetration occurs and,

consequently, sets the absolute minimum resolution. The resolution is also affected by an intrinsic uncertainty in determining the incident photon position due to statistical variations in the PMTs output signals and due to contributions from multiple photon interactions. A gamma camera with a parallel-hole collimator also exhibits a distance-dependent resolution, i.e., the distance between the emission point and collimator impacts the resolution as photons can pass more holes when the source-to-collimator distance increases. Additionally, septal penetration, wherein the finite thickness of the septum will not be able to stop all photons and results in the detection of events that are not parallel with the collimator holes, which also affects the spatial resolution.

Hence, the collimator design is, ultimately, a compromise between spatial resolution and sensitivity, with clinical gamma camera systems typically exhibiting worse spatial resolution than clinical PET systems (Alqahtani et al. 2022).

Partial Volume Effects

Limited spatial resolution has an impact on the quantitative capabilities as signal from different sources may blur together (Kojima et al. 1989). These spatial resolution-related effects are referred to as partial volume effects (PVEs). In these cases, the principal component of PVE arises from apparent cross-contamination of activity between adjacent regions, i.e., the activity appears to spill over from one volume to another (Erlandsson et al. 2012). Partial volume effects may further be exacerbated by temporal factors and, consequently, patient motion, respiratory motion, or heartbeat can introduce additional PVEs.

For an object situated in a background with lower activity concentration, the PVE smears out its signal. The consequence of this is that the apparent activity concentration in the object will be lower than the actual activity concentration while also making the object appear bigger. Conversely, if the object is situated in a background with higher activity concentration, the object's activity concentration will be overestimated. The effects of PVEs are typically small centrally in objects whose diameter is more than three times larger than the FWHM of the system's point spread function (i.e., the image of a point source which characterises a system's resolution) (Soret et al. 2007). However, spill-out is partly compensated by the fact that activity from outside the object will spill-in. The PVE is complicated to compensate for, as the balance of spill-in and spill-out depends on the relation between the object and the surrounding activity concentration.

Compensation for PVE can be done by incorporating resolution modelling during the reconstruction with the aim of reversing the effect of the point spread function. While resolution modelling produces resulting images that can suffer from the undesirable introduction of Gibbs artefacts, (Tong et al. 2011, Erlandsson et al.

2012), introducing resolution modelling improves the resulting images both qualitatively and quantitatively (Tsui et al. 1994, Reader et al. 2003).

A simpler method to compensate for PVEs is to utilise image-based recovery coefficients (RCs) (Kessler et al. 1984). The RCs can be defined as the ratio of apparent activity concentration to the true activity concentration, and the simplest method is to calculate the recovery coefficients through phantom measurements with spheres of various sizes in a cold background (i.e., non-radioactive) by directly comparing the fraction of activity recovered after reconstruction from volumes-of-interests matching the physical size of the spheres to the known amount. The RCs then attempt to recover the activity lost due to PVE to provide a better estimate of activity concentration in individual objects. While this method only compensates for spill-out of counts from hot to cold regions, which inherently neglects spill-in of counts, spill-in can be compensated for. However, this, requires more effort, as the RCs are dependent on the target-to-object activity-concentration ratio (Srinivas et al. 2009).

Sensitivity

High sensitivity is important to reduce the effects of statistical fluctuations and its propagation to the reconstructed image. However, emission tomography often suffers from low sensitivity as a large portion of the imaged object is typically located outside the scanner's FOV during imaging, and for the portion located within the scanner's FOV, only a small fraction of the emitted photons are detected (Daube-Witherspoon and Cherry 2021).

Positron emission tomography typically exhibits higher sensitivity due to larger usable acceptance angles compared to the gamma camera, which is limited by geometrical restrictions imposed by the collimator (Rahmim and Zaidi 2008). Consequently, the choice of collimator is a balance between spatial resolution and sensitivity for gamma cameras. Gamma camera imaging nevertheless has the advantage of utilising radionuclides with a longer half-life, and is thus able to study slow physiological processes, which is not readily possible with PET (Meikle et al. 2005).

The sensitivity in PET is contingent on the properties of the scintillator crystals (Eriksson et al. 2007, Daube-Witherspoon and Cherry 2021), e.g., crystal size and linear attenuation coefficient. Pertaining to this matter, the use of fast detectors to incorporate TOF measurements effectively results in an improved signal-to-noise ratio equal to $\sqrt{D/\Delta x}$ compared to non-TOF measurements, where D is the diameter of the imaged object and Δx is the uncertainty in spatial localisation of the event along the LOR and is given by $\Delta x = c\Delta t/2$ where Δt is the coincidence timing resolution, and c is the speed of light (Budinger 1983).

The higher sensitivity and spatial resolution have prompted a shift in certain nuclear medicine exams towards PET, where the radiopharmaceutical permits the change to a PET-compatible isotope (Miller et al. 2022), e.g., from planar ^{111}In scintigraphy or ^{111}In-SPECT to ^{68}Ga-PET for neuroendocrine tumour imaging (Buchmann et al. 2007, Lee et al. 2015).

3. Tomographic Reconstruction

Tomographic reconstruction is a vital component in numerous diagnostic medical imaging procedures. The externally measured data in nuclear medicine consist of coincidences (PET) or single events detected within the primary energy window (SPECT). The fundamental desire is to map the data acquired from the imaging procedure back to its point of origin.

In practice, the task is to translate the measured data into a discretised finite image matrix representing the three-dimensional radiopharmaceutical distribution that generated the measured data. Hence, following a nuclear medicine imaging acquisition, the primary objective is to invert the projection acquisition process. Mapping the measured data back to its origin thus enables a straightforward interpretation of whether the observed data can be attributed to normal or pathological mechanisms.

A volumetric image can be considered a stack of two-dimensional images, and the two-dimensional reconstruction case will be considered for the section covering the analytical reconstructions. However, the two-dimensional case is analogous to the three-dimensional.

Analytical reconstruction

The measured signal of a parallel projection, p, acquired at an angle φ, can be thought of as the integration of signals originating from an object represented by the function $\theta(x, y)$ along straight lines defined by the position s,

$$p_{\varphi}(s) = \int_{-\infty}^{\infty} \theta(x, y) dr. \tag{3.1}$$

Equation (3.1) represents a point in projection space and is known as the Radon transform of the object function, $\theta(x, y)$ (Kak and Slaney 1988). For analytical reconstruction, the goal is to invert the Radon transform to recover the object function from the measured projections. Recovering the object function from the projections is possible, provided a continuum of projections can be measured over the interval $\varphi \epsilon [0, \pi)$.

A first intuitive attempt to recover the object function from the projection would be to uniformly distribute the signals from the projections back along the straight lines for all angles. While the signals are allocated about their point of origin, it also misallocates signal along the straight lines. This method is known as direct back-projection and results in a blurred representation of $\theta(x, y)$.

The uniform allocation of signal along the straight line can be rectified through filtration of the measured projections before back-projection. Employing a ramp filter (Shepp and Logan 1974) in the Fourier domain effectively mitigates the blurring resulting from direct back-projection, yielding a better estimate of $\theta(x, y)$. However, applying the ramp filter makes the result sensitive to high-frequency noise in the projection data, and, it is as such common to modify the ramp filter by a user-defined low-pass filter to de-emphasise higher frequencies (Lyra and Ploussi 2011). This reconstruction method with filtering prior to back-projection is referred to as filtered back-projection (FBP). Figure 3.1 shows the difference between inverting the Radon transform using direct back-projection and FBP for a noise-free Shepp-Logan phantom.

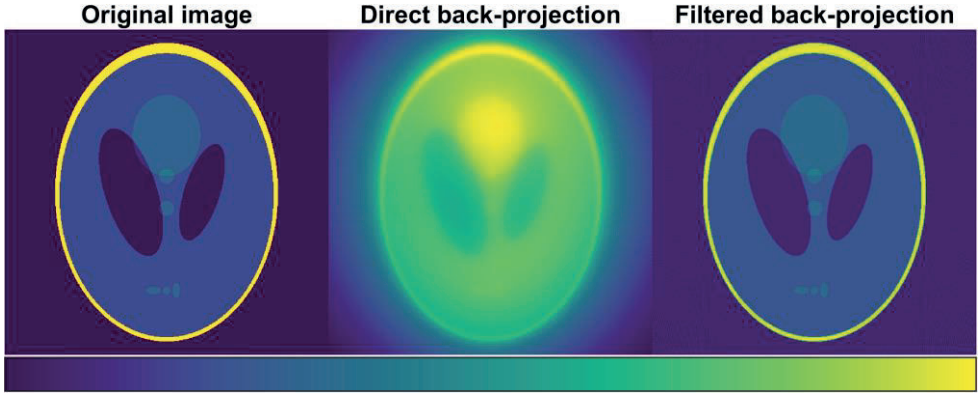

Figure 3.1: Difference between direct back-projection and FBP (ramp-filter only). While the overall structure is recovered, the blurred representation of the object function results in the loss of fine details, rendering the direct back-projection unusable. Filtered back-projection manages to recover a highly detailed representation of the object function.

Filtered back-projection has been the prevailing approach for tomographic reconstruction due to its computational speed (Bruyant 2002). However, regarding the expression presented in equation (3.1), analytical reconstructions are limited as they cannot readily compensate for image-degrading effects. Attempting to include such effects would result in a highly complex function, making analytical inversion challenging to generalise (Frey and Tsui 2006). This limitation is more pronounced in SPECT, where projections cannot be pre-corrected to the same extent as in PET.

Notwithstanding, FBP reconstructions are often hampered by streaking artefacts due to a limited number of angles acquired in practice.

Iterative reconstruction

The assumption that a unique solution through inversion of equation (3.1) exists does not hold in practice due to noise. Consequently, there are either no solutions or an infinite number of solutions to the reconstruction problem, and the challenge is instead shifted from finding a unique solution to finding the 'best' solution of $\theta(x, y)$ based on the measured projections.

Iterative reconstruction algorithms are well suited to solving systems of linear equations and can thus be a suitable option in the attempt to estimate the 'best' solution. An iterative algorithm contains a feedback process, so a current estimate is sequentially adjusted, and each update attempts to improve the conformity between the projections of an estimated object function and the measured projections. The intuitive assumption is that if the conformity between the projections of the estimated object function and the measured projections is high, then the conformity between the estimated object function and the true object will also be high.

The distinct advantage of iterative reconstructions is their capability to compensate for image-degrading elements during reconstruction, and the introduction of iterative reconstruction algorithms has significantly improved reconstructed image quality (Wilson and Tsui 1993, Leahy and Qi 2000). Moreover, as computational capabilities have improved, the clinical implementation of iterative reconstruction algorithms has become increasingly more feasible.

Iterative reconstructions are constructed based on a linear model (Qi and Leahy 2006), with the linear model connecting the measured projections to the object function via a system matrix (in matrix notation),

$$\boldsymbol{p} = \boldsymbol{A\theta}, \tag{3.2}$$

where $\boldsymbol{p}$ are the measured projections, $\boldsymbol{\theta}$ represents the object function, and $\boldsymbol{A}$ is the system matrix. The system matrix describes the physical models governing the emission and detection process. Essentially, each element, a_{ij}, of $\boldsymbol{A}$ describes the probability that an event originating from location j will be detected in sinogram bin i. The probability of the elements within the system matrix depends on various factors, such as non-uniform sensitivity and attenuation.

The 'best' solution is contingent on the criteria employed to evaluate whether the 'best' solution has been reached, i.e., the metric by which a cost function determines conformity between the measured projections and the projections of the estimated object function (Qi and Leahy 2006). As stated, either no solution or an infinite number of possible solutions exist due to the inherent presence of noise in emission

tomography. We therefore aim to estimate an object function based on a model of the mean of the measured data, i.e., $\boldsymbol{q} = \boldsymbol{A\theta}$. One implementation of the cost function can be defined by maximising the likelihood under the assumption of Poisson-distributed noisy data. The likelihood that the mean is q_i for a measure of p_i counts for a given projection bin i, or the probability that we measure p_i counts given a mean q_i, is

$$\mathrm{L}(\boldsymbol{\theta}|\boldsymbol{p}) = \prod_{i=1}^{I} \Pr(p_i|q_i(\boldsymbol{\theta})) = \prod_{i=1}^{I} \frac{q_i^{p_i}(\boldsymbol{\theta}) e^{-q_i(\boldsymbol{\theta})}}{p_i!}. \tag{3.3}$$

Hence, we seek to find an object function with the highest probability of generating $\boldsymbol{p}$, or equivalently, find the object function that maximises the likelihood. For simplicity, we will estimate the Poisson log-likelihood rather than the Poisson likelihood (which is acceptable considering that the maximum occurs simultaneously given that the logarithmic function is monotonic),

$$\Lambda(\boldsymbol{\theta}|\boldsymbol{p}) = \sum_{i=1}^{I} p_{\mathrm{i}} \ln\big(q_{\mathrm{i}}(\boldsymbol{\theta})\big) - \sum_{i=1}^{I} q_{\mathrm{i}}(\boldsymbol{\theta}). \tag{3.4}$$

As the object function $\boldsymbol{\theta}$ changes, so will the scalar value of Λ. The method by which Λ is maximised can vary, but one approach is the expectation-maximisation (EM) algorithm (Dempster et al. 1977). The maximum-likelihood expectation-maximisation (ML-EM) algorithm under the assumption of Poisson-distributed data (Lange and Carson 1984) can be expressed as,

$$\theta_j^{k+1} = \frac{\theta_j^k}{\sum_{i=1}^{I} a_{ij}} \sum_{i=1}^{I} a_{ij} \frac{p_i}{\sum_{j=1}^{J} a_{ij} \theta_j^k}. \tag{3.5}$$

The ML-EM algorithm begins with an initial object function estimate, θ^0, often a positive uniform image. The iterative process then proceeds by forward-projecting the current image estimate. The measured data and the forward-projected current estimate are compared, whereby the ratio between the measured data and the forward-projected estimate is back-projected (i.e., the propagation of the ratio back to image space) and normalised by the sensitivity image $\left(\sum_{i=1}^{I} a_{ij}\right)$. The current estimate is then updated via element-wise multiplication of the normalised back-projected ratio. This process is performed for a specified number of iterations. The process of the ML-EM algorithm is illustrated in Figure 3.2.

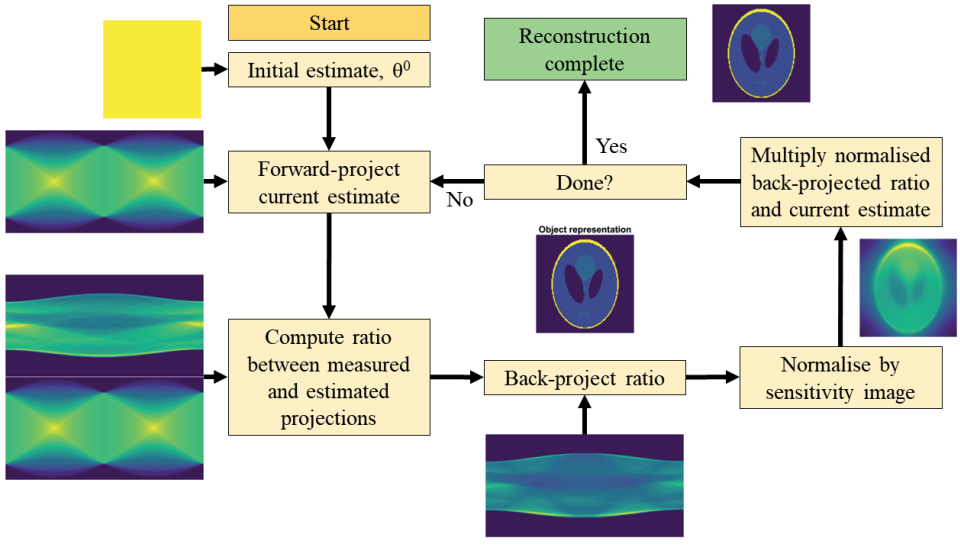

Figure 3.2: Flowchart of the iterative ML-EM process. The initial estimate (yellow box) typically consists of a positive uniform image. The algorithm will continue to update the current estimate until a predefined number of iterations has been performed.

There are some limitations to the ML-EM algorithm. The convergence by which structures are formed is not independent of object size and its neighbouring structures, with smaller objects necessitating more iterations to reach convergence than larger ones (Liow and Strother 1993). Thus, the number of iterations typically used to reach convergence is large, which escalates the propagation of image noise (Barrett et al. 1994, Wilson et al. 1994). This interplay between convergence and noise ultimately leads to a point at which the algorithm must be terminated manually. Determining the stopping point involves finding a balance between reaching convergence and maintain adequate image quality, and the point at which the algorithm is stopped is often decided based on previous experience. Nonetheless, methods to introduce quantitative criteria to stop iterations have been made by evaluating an objective metric to limit image deterioration due to over-iterating (Veklerov and Llacer 1987, Gaitanis et al. 2010). Figure 3.3 shows an example of the Shepp-Logan phantom without noise reconstructed with 1, 3, 10, 20, and 200 iterations.

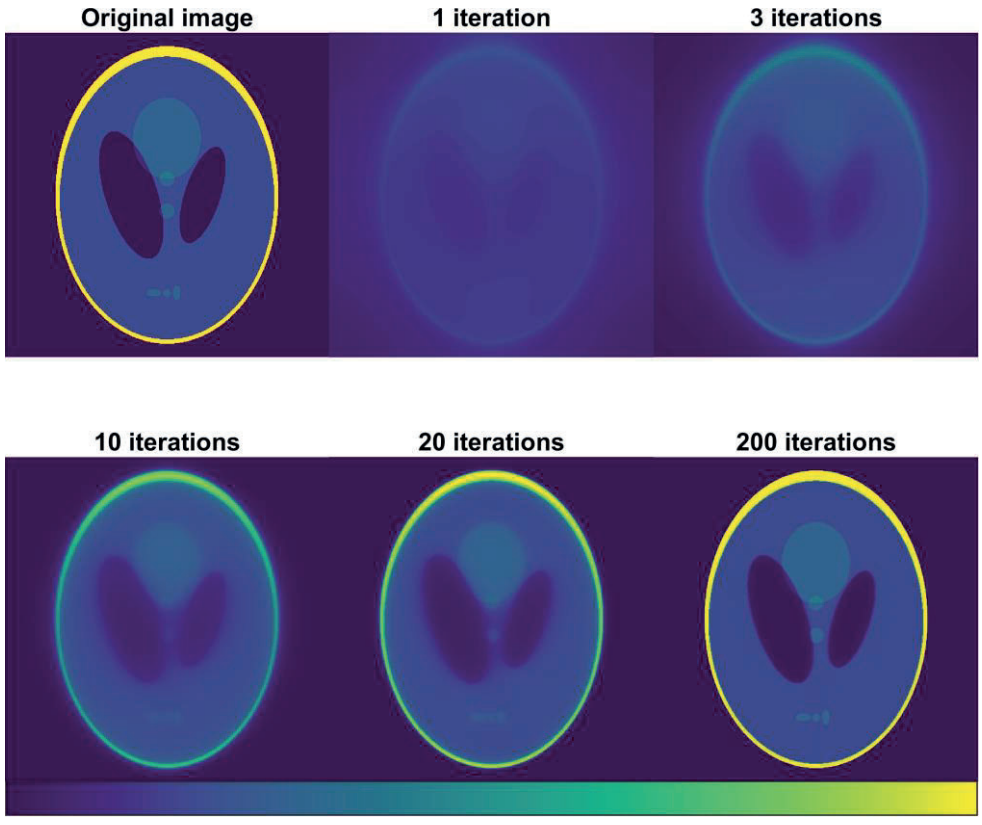

Figure 3.3: ML-EM reconstruction stopped after 1, 3, 10, 20, and 200 iterations. After a few iterations, the general features of the original image are recovered. The ML-EM algorithm requires more iterations to adequately resolve the smaller fine details.

Since the ML-EM algorithm uses all measured data during every iteration, the process is slow-paced as the forward-projection and back-projection steps are computationally demanding. One method to expedite the reconstruction process is to only use a subset, S_l, of the complete dataset to update the current estimate of the object function, as the image quality is typically contingent on the number of updates rather than iterations (Kamphuis et al. 1996). This method of accelerating the ML-EM algorithm is known as the ordered-subset expectation-maximisation (OS-EM) algorithm (Hudson and Larkin 1994),

$$\theta_j^{k+1,l} = \frac{\theta_j^{k,l}}{\sum_{i \epsilon S_l} a_{ij}} \sum_{i \epsilon S_l} a_{ij} \frac{p_i}{\sum_j a_{ij} \theta_j^{k,l}}. \tag{3.6}$$

If the product of subsets and iterations equals the number of ML-EM iterations, the solution closely approximates the ML-EM estimate. However, it is worth noting that there is no proof that the OS-EM estimate converges to the same estimate as ML-

EM or that it converges at all. Nevertheless, with noisy data typically encountered in clinical practice, this issue is not of particular concern (Hutton et al. 2006, Qi and Leahy 2006). While OS-EM has theoretical limitations, its superior speed makes it favourable over ML-EM in clinical practice.

The ML-EM and OS-EM adaptation is one way to estimate the object function from the measured projections. Other implementations of the cost function exist, with one popular algorithm being the block-sequential regularised expectation-maximisation (BSREM) (De Pierro and Yamagishi 2001, Ahn and Fessler 2003). The BSREM is a globally convergent algorithm that maximises a penalised version of the likelihood.

While iterative reconstruction algorithms dominate clinical practice, analytical reconstructions are still useful. The implemented scatter correction (Paper I) uses analytical reconstruction techniques to reconstruct an initial source distribution. The main reconstructions in Papers I-IV were performed using the OS-EM algorithm.

4. The Monte Carlo method

The Monte Carlo method is a probabilistic numerical technique that can be used to solve non-deterministic problems. Monte Carlo simulations rely on sampling random numbers to predict outcomes from known probability distributions associated with mathematical models representing physical systems. Monte Carlo simulations have proven valuable due to their inherent capability for handling the stochastic nature of radioactive decay, particle transportation, and detection in nuclear medicine (Zaidi 1999, Buvat and Castiglioni 2002). Monte Carlo simulations are especially useful when the problem's dimensionality escalates, e.g., the computational time to analytically simulate every particle interaction quickly becomes practically unmanageable.

The core of MC simulations relies on the generation of uniformly distributed random numbers. While truly random numbers are impractical for computational purposes, pseudo-random number generators, which produce a sequence of numbers that appears random but is deterministic, are instead used in practice. Pseudo-random number generators will always generate the same sequence of numbers when given an initial starting seed. Several sophisticated algorithms are available for generating random numbers, such as RANLUX (James 1994), RANECU (Lecuyer 1988), and Mersenne Twister (Matsumoto and Nishimura 1998).

In this context, a simulation primarily focuses on transporting and detecting particles within structures based on object-dependent relationships. These object-dependent relationships are expressed as probability density functions (PDFs) and describe the likelihood of a particular interaction occurring. The PDFs are sampled based on the randomly generated number, and the simulation selects one of many possible outcomes. This process continues until the particle comes to rest or exits the simulation-world boundary. Individual outcomes or trajectories within the simulation are referred to as histories, and simulating multiple histories is necessary to obtain accurate estimates of the studied parameters. As more histories are simulated, the results approach the system's average, converging to the expected value as the number of histories approaches infinity.

The realisation of the usefulness of simulations may stem from the ability to create multiple instances of the same study with minor variations. With users in control of the input data driving the simulations, tracking deviations resulting from modifications to the input data becomes straightforward (Fahey et al. 2018).

Consequently, constructing imaging systems within the simulation world allows for the modelling of particle detection, enabling the replication of clinical imaging systems and exams. This complete control over the simulation enables the study of parameters that are inseparable in studies with physical phantoms or clinical exams. However, it is important to note that while the MC method is exact in the limit of infinity with respect to the number of simulated histories, the results of the simulation will still depend on the accuracy of the models used to represent the physical systems and the accuracy of the modelled imaging system.

Numerous suitable MC programs are available for applications in nuclear medicine (Jan et al. 2004, Ljungberg and Strand 1989, Sempau et al. 1997). Monte Carlo programs are generally divided into general-purpose programs and specialised programs, and the choice of MC program depends on the user's specific needs, as each has advantages and disadvantages (Buvat and Castiglioni 2002, Zaidi 2022). The studies underlying this thesis used two MC software programs: GATE[3] (Jan et al. 2004) to simulate PET and SIMIND[4] (Ljungberg and Strand 1989, Ljungberg 2012) to simulate SPECT. Although both GATE (**Papers I–IV**) and SIMIND (**Papers III–IV**) were utilised, the focus of this chapter will primarily be on GATE due to personal experience with this tool. Hence, a more detailed description of GATE will be provided, along with a brief description of SIMIND.

GATE

The GATE MC software (Jan et al. 2004) is built on top of the Geant4 kernel (Agostinelli et al. 2003), and GATE offers extensive capabilities for the simulation of various medical physics-related applications.

A GATE simulation is built through a series of macro commands defined in plain text files, which is subsequently provided to the GATE engine. Using macro commands simplifies the learning process and eliminates the need for C/C++ programming experience. Each GATE simulation comprises four fundamental components: *geometry*, *physics*, *source*, and *actors*.

The *geometry* component describes the solid components within the simulation, such as detectors, phantoms, and collimators. These solid components can be represented in various ways, including voxel matrices, meshes, and analytical descriptions, enabling the modelling of complex geometrical shapes. Each solid element must be assigned material composition and density through a dedicated material file.

[3] Web page: http://www.opengatecollaboration.org/

[4] Web page: https://www.msf.lu.se/en/research/nuclear-medicine-group/software/simind-monte-carlo-program

The *physics* component provides the physical models used during the simulation, including particle interaction cross-section databases and definitions for particle cuts. Particle cuts refer to a distance threshold below which no secondary particles are produced. The *physics* component also encompasses the equations and data associated with specific physical interactions. The underlying models and options are sourced from Geant4, which offers well-validated and up-to-date databases and physics interaction models.

The *source* component handles the creation and tracking of particles from their inception. Multiple source types are available within GATE, ranging from simple pencil-beam sources to complex three-dimensional distributions.

Lastly, *actors* serve as a tool to engage with the simulation. In this thesis, as anatomical imaging was not explicitly simulated, an actor was employed to generate images containing linear attenuation coefficients of the simulated phantoms. These images were later used to compute attenuation-correction factors and within the SSS algorithm for scatter correction.

Phantoms can be represented using three-dimensional matrices or a combination of analytical geometric primitives. If the voxel-based method is chosen, an explicit descriptor file that associates voxel values with material composition must be created. Geant4 uses a hierarchical structure for describing solid objects, where a parent volume must entirely encompass a daughter volume. This means that volumes cannot overlap, which can pose challenges in certain scenarios. For instance, when describing a phantom using a voxel matrix, there is a significant risk that the matrix's edge will overlap with the volume of the detector system. Figure 4.1 shows a phantom created using geometrical primitives and a voxel-based phantom positioned within a PET scanner.

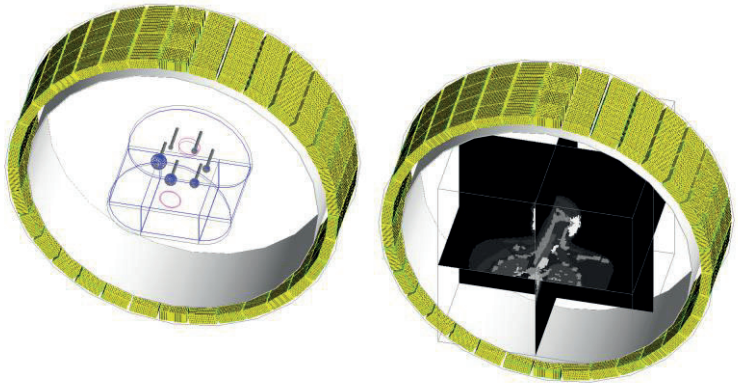

Figure 4.1: Two different modes of phantom representation in GATE. The combination of geometrical primitives strategically arranged to create the NEMA IQ phantom (left). Volumes within other volumes must be declared as daughter volumes and be entirely encompassed by the parent volume to avoid any volume overlap conflict. Voxel-based phantom representation (right).

In PET simulations, avoiding overlap between a voxel-based phantom and the arc of detectors can be challenging. One solution to this issue is to crop the phantom matrix by removing non-contributing voxels, particularly those representing air. Alternatively, the simulation can be conducted in two stages. First, the simulation runs without detectors, and particles exiting the phantom are recorded and stored in the surrounding volume. In the second stage, detectors are introduced and the phantom removed, and the simulation resumes using the previously recorded data as a starting point.

The method for particle tracking varies depending on the phantom description. In the case of voxel-based phantoms, dedicated navigation algorithms are used to improve simulation efficiency rather than standard navigation within generic volumes. The computational acceleration is achieved through customised tracking algorithms that reduce the number of steps at voxel boundaries (Sarrut and Guigues 2008).

While the Geant4 kernel handles the physics models, the GATE engine is responsible for sampling particle position, direction, energy, and type from specified distributions. The initial spatial source distribution can be described using analytical models or voxel matrices. For voxel-based source distributions, an explicit descriptor file must be provided, associating voxel values with an activity concentration in units of [$Bq \cdot vox^{-1}$]. In some applications where a distinct particle is desired, the most efficient simulation is to generate only the last-stage particle, such as the back-to-back emission of annihilation photons. Alternatively, the more versatile, albeit slower, approach is to simulate the entire decay chain of any ion directly.

Lastly, the detector and its response chain must be modelled for the GATE simulation to be applicable in nuclear medicine imaging. This part consists of two steps: modelling the physical detector geometry and modelling the processes that account for how particle interactions within the detector elements are translated into a recorded signal.

The solid elements of any detector, such as the scintillator crystals, are created using analytical geometric primitives. Tools are available to ease and streamline the creation of scanner systems within GATE.

The signal processing module, known as the digitizer, simulates the front-end electronics of a signal processing chain. Users construct the digitizer module by selecting a series of processing modules to manipulate the list of interaction events recorded in the detector elements. This process chain allows for modelling of spatial, energetic, and temporal uncertainties, thus enabling the simulation of various constraints inherent in a clinical scanner. Moreover, the Geant4 engine assigns timestamps to all particles and interactions, facilitating timing-related tasks such as coincidence detection and time-of-flight measurements.

GATE makes it feasible to simulate complex and highly realistic scanner settings with relative ease. However, once a system has been constructed, validation of the model by comparing simulation results with experimental data becomes crucial. Yet, accurately representing a clinical scanner is contingent on obtaining precise information about the scanner, and access to such information often necessitates non-disclosure agreements, rendering validation processes an ongoing challenge.

The GATE model and its connection to a stand-alone reconstruction software program were validated in Paper I. The validation of the computational chain allows for subsequent simulation-based studies to be conducted and increases confidence in the model's ability to accurately generate results akin to those of the replicated clinical scanner.

SIMIND

SIMIND (Ljungberg and Strand 1989, Ljungberg 2012) is a specialised photon transport software program for simulating planar gamma camera imaging or SPECT. In recent developments, SIMIND has been extended to include the simulation of solid-state cadmium zinc telluride (CZT) cameras (Pretorius et al. 2015, Roth et al. 2022). Moreover, to improve computational efficiency, SIMIND incorporates multiple variance-reduction techniques. Variance-reduction techniques alter the probabilities during the simulation to improve computational efficiency, e.g., restricting the sampling of emissions to only simulate photons impinging the detector. Consequently, due to the extensive use of variance-reduction techniques, the resulting counts in the projections do not follow a Poisson distribution. It is therefore advisable to continue the simulation until the projections are essentially

noise-free and then introduce Poisson-distributed noise. Like GATE, SIMIND enables simulations of voxel matrices, allowing for the modelling of highly intricate geometries and source distributions.

The [^{177}Lu]Lu-DOTA-TATE SPECT simulations in **Paper III** and **Paper IV** were performed using SIMIND.

5 Anthropomorphic patient models

The precise models of Monte Carlo simulations enable the simulation of clinical applications, with one advantage of Monte Carlo simulations is the ability to isolate and manipulate individual parameters. Once the simulation model accurately replicates the camera system, it becomes possible to disentangle the effects of *in vivo* confounders *in silico*.

In many nuclear medicine applications, simple geometric phantoms, e.g., spherical or cylindrical phantoms, may be sufficient (ICRU 1992). However, our ability to study phenomena occurring during a nuclear medicine exam, whether through physical measurements or simulations, is limited by the simplicity of these phantom models. A basic geometric phantom with a set of hot and cold spheres does not adequately represent the intricacy of human internal structures.

Consequently, regardless of the imaging system model's accuracy in representing a clinical scanner, the lack of phantom complexity may lead to a discrepancy between simulations and clinical measurements, resulting in an insufficient representation of the studied phenomena. This effectively limits the range of practical uses in which the obtained results can be applied. To address this limitation, anthropomorphic patient models have been introduced to enhance the realism and reduce the complexity gap between simulations and clinical exams.

Early anthropomorphic phantoms were constructed using geometric primitives arranged strategically to mimic organs and overall body shape. Snyder et al. (1978) developed initial versions of these stylised anthropomorphic phantoms, which were later adapted to resemble children and pregnant women (Cristy 1980, Stabin et al. 1995). While these phantoms offered flexibility by allowing changes to organ representations, they still fell short of achieving adequate patient realism.

Voxelised phantoms, based on segmented patient images, were therefore developed to further enhance the patient models (Zubal et al. 1994). This approach offered significantly higher anatomical realism. However, these voxel-based phantoms demand time-consuming image segmentation (Caon 2004), which limits the creation of extensive databases to represent the anatomical variability found in patient populations.

Hybrid phantoms have emerged to address the need for highly realistic patient-resembling geometries while allowing for the rapid creation of a diverse phantom

population (Segars et al. 2010, Kim et al. 2011, Lee et al. 2007). Hybrid phantoms combine concepts of mathematical and voxel-based principles, utilising non-uniform rational B-splines (NURBS) or polygon meshes to define the phantoms' organ surface contours (Kainz et al. 2019). This surface representation retains anatomical realism and provides flexibility for altering the size and shape of organs by modifying the NURBS via control points.

The XCAT phantoms (Segars et al. 2010) are hybrid models that use NURBS to represent organ surfaces. With this feature, a single phantom can generate multiple variations of itself, making it well-suited for mimicking organ motion through deformations and transformations. Hence, these phantoms can be generated at different respiratory and heart stages once the deformations and temporal translations have been defined. The XCAT phantoms were initially based solely on the segmentation of the Visible Human dataset (Ackerman 1998), which was not considered sufficiently flexible to capture the anatomical variability of a patient population. Over time, the XCAT population has expanded to include 58 unique phantoms (Segars et al. 2013). Figure 5.1 shows three different hybrid phantoms from the XCAT population.

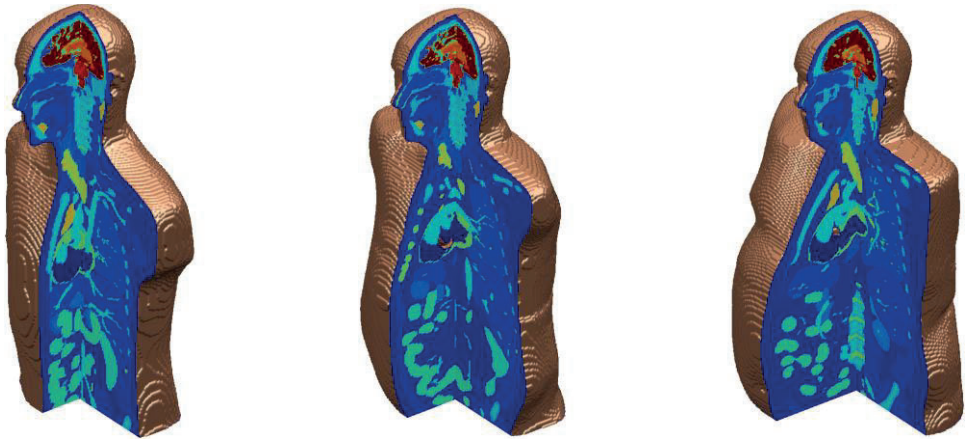

Figure 5.1: Three distinct variations of hybrid computational human phantoms generated from the XCAT population.

Using highly realistic anthropomorphic phantoms enables the close emulation of patients *in silico*. These improved patient models are better suited for simulating clinical nuclear medicine exams due to their increased complexity. This enhanced complexity facilitates the interplay of anatomical and physiological intricacies inherent in patients to be modelled, and avoids the limitations imposed by simple geometric phantoms. When combined with MC simulations, anthropomorphic

phantoms can help address the challenge of determining the most suitable approach to maximise standard of care for a particular medical exam (Zhang et al. 2014, Brolin et al. 2016, Fu et al. 2017). Physical phantoms are constrained in this regard, as it is neither feasible nor cost-effective to produce a comprehensive range of patient sizes, variations, and deformations to cover the inherent anatomical variability among patients.

Anthropomorphic phantoms were used in Papers (II–IV), with the patient model realism improved in ascending Paper order.

6. A Tool for Systematic Evaluation

Improving the efficiency and quality of medical imaging exams is crucial, and conducting MC simulations can help achieve this goal. To ensure reliable and relevant results following an MC simulation, the use of realistic patient models and an accurate imaging system model is essential. However, it is vital to reconstruct the simulated projections to make the simulation results clinically relevant, as the end product of a diagnostic medical imaging exam is, after all, the tomographic reconstructed image. Consequently, it is equally important that this step emulates the clinical system's reconstruction procedures.

A tool connecting simulations of nuclear medicine imaging systems and realistic patient models to a reconstruction software is thus a powerful approach for investigating clinically relevant issues. Such a pipeline, used in this thesis, can be divided into three components: the scanner model, the patient model, and the reconstruction software. **The validation of this pipeline is described in Paper I.** Below is a description of the efforts taken to improve the correspondence of the results from the pipeline with the results from clinical measurements.

Scanner model

The GATE scanner model is based on the Discovery MI (GE Healthcare, Milwaukee, WI) PET scanner with a 20 cm axial FOV. Steps were taken to replicate the scanner's geometrical configuration and its front-end electronic settings. While the geometrical configuration can often be constructed piece by piece using published information (Chicheportiche et al. 2020, Oddstig et al. 2021) or through information obtained from the vendors, modelling the front-end electronics tends to be more challenging.

Information about every constituent of the clinical scanner is not readily available, and some functionalities, such as Compton scatter recovery (Wagadarikar et al. 2014), available in Discovery MI PET scanners, are not implemented in GATE. Hence, parts of the scanner model will not exactly replicate the clinical scanner. Moreover, saturation of silicon photomultipliers (SiPM) is typically low at the activity levels found in clinical PET exams (Wagatsuma et al. 2017, Gonzalez-Montoro et al. 2022), and deadtime was therefore not incorporated within the GATE model. These omissions are effectively equivalent to an idealised rejection of these

phenomena, and while such omissions will ultimately affect the model's correspondence with the replicated scanner, their overall impact is considered small. Instead, one must consider the practical trade-offs between model complexity and the time required to implement the additional features.

In this context, perfect estimations of correction factors can be made based on the availability of underlying data following MC simulations. However, acquiring correction factors in this manner leads to an idealised correction, which is not attainable in a clinical setting. Therefore, substantial efforts were made to implement programs for computing correction factors as performed in a clinical scanner (see Chapter 2.).

For a comprehensive explanation of the scanner model, refer to **Paper I**.

Patient model

Nuclear medicine imaging is always conducted with a specific objective in mind, such as lesion detection, determining activity concentration within tissue, or classifying pathology. In emission tomography, statistical noise often limits the performance of these tasks. However, for a given task, the relative impact due to noise will saturate at some point as the time-activity product increases. In those cases, the limiting performance of the task is instead set by the intrinsic randomness within the imaged object (Barrett 1990).

Hence, the structural intricacy within an overtly simple geometry may not adequately represent to the anatomical complexity inherent in patients and the intricate physiological mechanisms responsible for the radiopharmaceutical's distribution cannot be emulated. Evaluating the performance of certain tasks based on simple geometric shapes may therefore be inadequate. Hence, to ensure unbiased estimation of task performance, the simulation, including the patient model, should reflect the complexity of the emulated measurement. For instance, typical assumptions, such as patient models with uniform intra-organ activity concentration, represents a simplification of the inherent complexity found in a clinical setting, and such oversimplification could potentially impact task performance assessment (Rolland and Barrett 1992, Eckstein et al. 1997).

While the omission of individual components may not be the sole factor that deems a simulation adequately realistic or unrealistic, collectively neglecting multiple physical or physiological aspects can create a noticeably artificial appearance in simulated images and introduce biased results. Figure 6.1 illustrates how enhancing the realism of the patient model can improve the visual appearance of the image. Introducing more complexity within the simulated phantom aims to more closely replicate the intricacy in actual patients in order to counteract biased performance assessment following an MC simulation.

A methodology to improve the realism of computational human phantoms was developed in Paper IV.

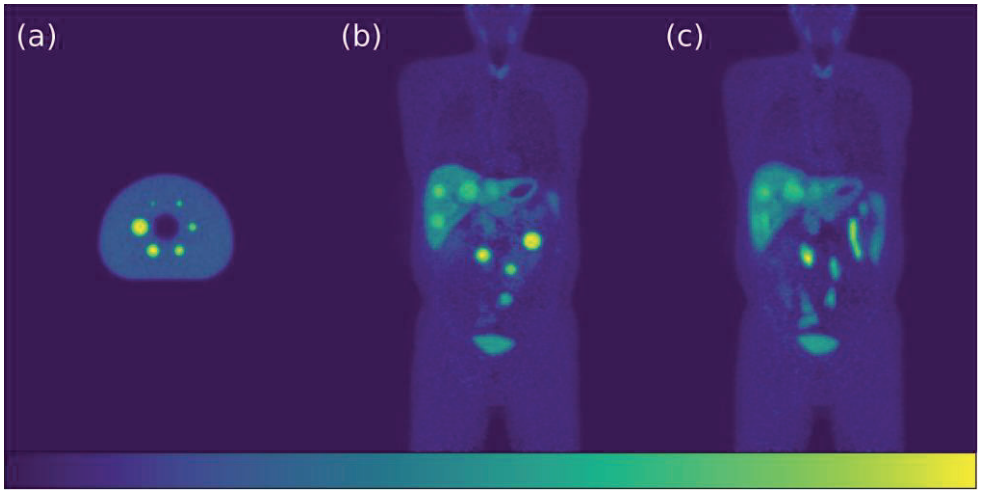

Figure 6.1: Reconstructed images following the simulation of three different patient models. The NEMA IQ phantom (a) may be sufficient to evaluate system performance, such as image quality. However, its geometrical simplicity cannot adequately represent the anatomical intricacies of an actual patient. The anthropomorphic phantom (b) represents an improved patient model that more closely replicates the complexity of a patient. The refined anthropomorphic phantom (c) incorporates respiratory motion, non-spherical lesions, and non-uniform intra-organ activity concentration to enhance the correspondence between the patient model and actual patients.

Coupling to Reconstruction

The work in this thesis employed the CASToR reconstruction software (Merlin et al. 2018) to establish a pipeline connecting PET MC simulations to quantitative reconstructed images. It is worth noting that other stand-alone reconstruction software, such as STIR (Thielemans et al. 2012) or OMEGA (Wettenhovi et al. 2021), could be considered for the construction of similar pipelines.

An accurate representation of the physical model, i.e., the system matrix, must be defined to obtain quantitative images. It is therefore essential to implement methods for the computation of correction factors (e.g., attenuation and normalisation) and effectively integrate them into the system matrix to compensate for these effects during the reconstruction process. The system matrix elements can be estimated in a few ways (Veklerov et al. 1988, Panin et al. 2006, Chen and Glick 2007). However, the complete data-set is typically extensive in modern PET scanners, so pre-computing and storing the system matrix becomes impractical. Implementations of iterative reconstruction algorithms therefore often employ ray-tracing algorithms to compute the system matrix on the fly.

The approach for estimating the system matrix elements in CASToR utilises ray-driven projectors (Joseph 1982, Siddon 1985, De Man and Basu 2004), where straight lines connect the detector elements in accordance with the scanner's geometry. No matrix elements are thus explicitly stored in memory, but are instead calculated, when necessary, by the reconstruction algorithm. The difference in projectors lies in how geometric aspects of the projection process are handled, and ultimately involves a trade-off between accuracy and computational efficiency.

Typically, the system matrix provides a detailed representation of the underlying physics involved in the imaging process. The system matrix can be factorised to describe various contributions of the image formation process (Rahmim et al. 2013, Qi et al. 1998). The linear model that describes the relationship between measured projections and the object function can further be expressed as

$$\boldsymbol{p} = \boldsymbol{A\theta} = \boldsymbol{NLX\theta} + \boldsymbol{s} + \boldsymbol{r}, \tag{6.1}$$

where $\boldsymbol{N}$ and $\boldsymbol{L}$ account for normalisation and attenuation losses, $\boldsymbol{X}$ represents the line integral, and $\boldsymbol{s}$ and $\boldsymbol{r}$ denote additive scatter and randoms contributions. Additional components, such as detector resolution, positron range, and photon accollinearity can typically be modelled in the system matrix to improve the representation of the physical model. Notwithstanding, the option to perform resolution modelling within CASToR is implemented as an image-based convolution with the point spread function (Stute and Comtat 2013). The CASToR framework incorporates scatter and random estimates in the forward-projection. By incorporating scatter and random contributions during the reconstruction process, the assumption of Poisson-distributed data is preserved, unlike when subtracting the data. Furthermore, data subtraction poses the risk of introducing negative bin values, which is incompatible with the non-negativity constraint imposed by the ML-EM algorithm.

The method employed for reconstructions in the studies underlying this thesis was list-mode reconstruction (Barrett et al. 1997, Reader et al. 1998) using the OS-EM algorithm. In list-mode reconstruction, each event is processed one by one as stored in the data file, as opposed to processing the data for each sinogram bin. The following occurs for each event retrieved from the list-mode file buffer: i) the system matrix elements associated with the event is computed and the object function is forward-projected; ii) the ratio between unity and the forward-projection is computed and back-projected. The key difference from equation (3.5) is that steps i) and ii) is performed for all recorded LORs rather than all possible LORs. After all LORs have been processed, the continuation of the algorithm is analogous with equation (3.5).

Time of flight measurements involve associating a time difference in the arrival of the two photons forming an LOR with a presumed spatial distribution of the annihilation site along the LOR. This is modelled by approximating the system matrix elements through the multiplication of independent TOF weights, i.e., the

TOF weights estimate the contribution of each voxel to a TOF bin. Consequently, the incorporation of TOF means that scatter and randoms estimates must also be adjusted to the associated TOF measurement. For randoms, this can be achieved by replacing the 2τ factor in equation (2.3) with the temporal width of the TOF bin, which is equivalent to dividing the non-TOF randoms estimate by the number of TOF bins. The method for estimating TOF scattered coincidences was covered in Chapter 2. For a comprehensive explanation of the CASToR TOF implementation, please refer to Filipović et al. (2019).

Figure 6.2 displays a transverse slice of a PET MC simulation reconstructed with CASToR using list-mode OS-EM, shown after every fourth update.

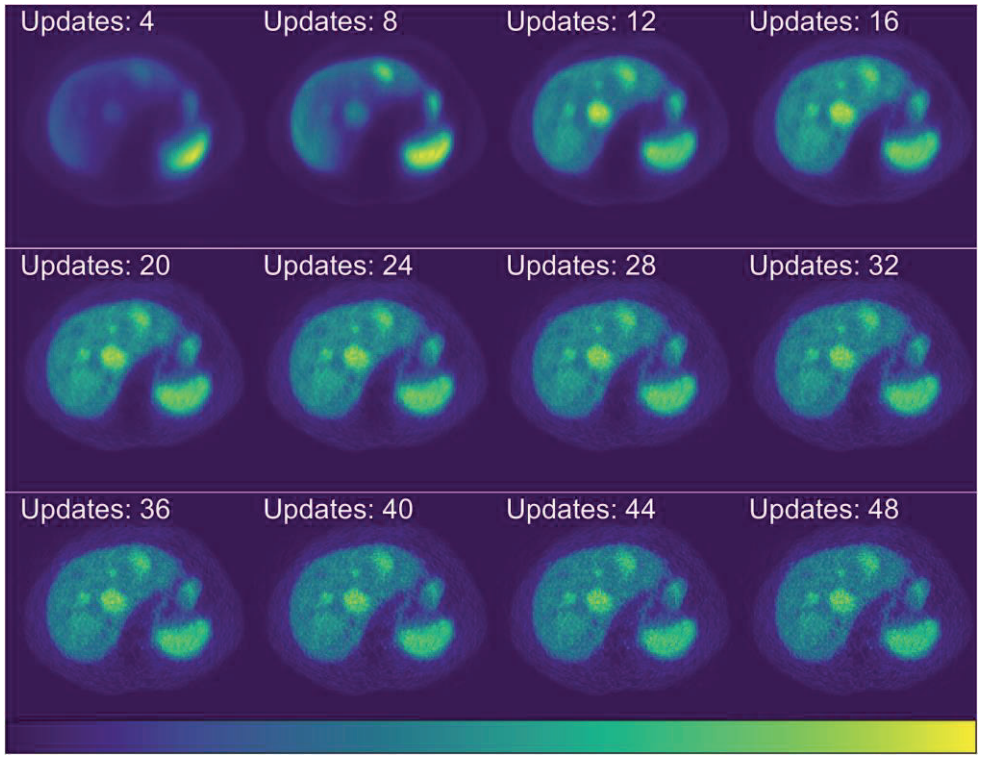

Figure 6.2: Transverse slices of a ^{68}Ga-PET simulation using an anthropomorphic phantom. The object function is relatively quickly recovered, and after 20 updates, the image does not substantially change.

The combination of an MC and a reconstruction software such as GATE and CASToR forms a tool that connects simulated data to reconstructed images. Access to the ground truth and the possibility to isolate parameters that are typically inaccessible in clinical measurements can improve our understanding of the issue at

hand. Therefore, this connection is desirable as it provides a method for systematically evaluating clinically relevant issues.

7. Clinical Applications

Theragnostics with ^{68}Ga PET and ^{177}Lu SPECT

Neuroendocrine neoplasms (NENs) are a group of heterogeneous tumours that can be divided into two categories: well-differentiated neuroendocrine tumours (NETs) and poorly differentiated neuroendocrine carcinomas (NECs) (Nagtegaal et al. 2020). The classification of NENs is an important prognostic marker, and it forms the fundamental basis for subsequent treatment stratification. Neuroendocrine neoplasms have a body-wide distribution, with the gastrointestinal tract and lungs being the most common primary sites (Oronsky et al. 2017).

Somatostatin receptors (SSTR) are ubiquitously expressed in the human body, with NETs commonly characterised by overexpression of SSTR frequency and density. It is estimated that at least 80% of NETs express SSTRs, while the SSTR expression is lower in NECs (Reubi and Schonbrunn 2013). The expression of SSTRs in NETs is often higher than in most normal tissues, a feature that can be exploited for imaging and therapy. Synthetic somatostatin analogues such as octreotide (DOTA-TOC) or octreotate (DOTA-TATE) can target NETs, with binding affinity depending on the somatostatin analogue and the cell SSTR subtype. Attaching a suitable radionuclide to the synthetic somatostatin analogue makes it then possible to visualise the radiopharmaceutical binding to SSTRs.

A widely used method for NET imaging is PET, using ^{68}Ga-labelled DOTA-conjugates, owing to its high sensitivity and specificity in lesion identification (Geijer and Breimer 2013, Deppen et al. 2016, Graham et al. 2017). These properties make [^{68}Ga]Ga-DOTA-radiopharmaceuticals appropriate for disease staging and therapy stratification (Sanli et al. 2018, Hennrich and Benesova 2020).

NETs with curative intent is primarily managed through surgical resection (Tsoli et al. 2019). However, surgical resection is typically restricted to tumours exhibiting slow progression (Schurr et al. 2007). Surgery may thus not always be a viable treatment option depending on metastasisation and the extent of metastases. Somatostatin analogues can then be used to systemically target NETs, where these acts as inhibitors for tumour growth. However, if tumour progression continues in spite of the somatostatin analogue treatment, then peptide receptor radionuclide therapy (PRRT) is an alternative approach (Baum and Kulkarni 2012). The concept is similar to ^{68}Ga-SSTR imaging, but it involves coupling a different radionuclide

to the synthetic somatostatin analogue with the intent of cell damage. This approach serves as a highly NET-targeting therapy, with ^{177}Lu being a common choice of radionuclide. The choice of radionuclides is limited, as the radiopharmaceutical's pharmacokinetic properties should not deviate too much from that of the imaging agent by the change of radionuclide. Nonetheless, the patient must have an SSTR-positive disease, as indicated by the ^{68}Ga-SSTR imaging, for ^{177}Lu-PRRT to be a viable NET-treatment option.

The use of molecular agents to identify patients who are likely to benefit from PRRT and the corresponding therapeutic agent for treatment is well-encapsulated by the term theragnostics (Frangos and Buscombe 2019), which embodies the concept that diagnosis and therapy are inherently interconnected. This combination of using molecular agents with equivalent targeting mechanisms means that the diagnosis can be followed up with personalised treatment (Baum and Kulkarni 2012).

In many cases, the patient selection for PRRT involves a qualitative evaluation of the ^{68}Ga-SSTR images, considering factors such as disease quantity, distribution, progression, and SSTR expression (Mittra 2018, Sanli et al. 2018). While there is generally high agreement in ^{68}Ga-SSTR PET interpretation, inter-observer variability still exists, leading to subjective patient selection for PRRT (Fendler et al. 2017). There is therefore interest in incorporating quantitative metrics into theragnostics to introduce objective criteria for evaluation, thereby strengthening the basis for PRRT selection, with efforts made to quantitatively and semi-quantitatively assess patient suitability for PRRT (Kratochwil et al. 2015, Werner et al. 2018). Such metrics are desirable within this theragnostic setting, for both predictive and prognostic indication. Other metrics, such as total tumour volume or total lesion somatostatin receptor expression (Tirosh et al. 2018, Toriihara et al. 2019, Abdulrezzak et al. 2016), have gained attention for evaluating prognosis and determining treatment stratification.

Similarly, quantitative metrics following serial peri-therapeutic SPECT imaging may also be beneficial. In this context, the estimation of absorbed doses is of interest, calculated based on serial peri-therapeutic SPECT imaging. The absorbed dose estimations would allow for tailoring of administered activity (or the number of PRRT cycles) such that an optimal absorbed dose is given to tumours while sparing normal tissue (Sundlöv and Sjögreen Gleisner 2021). Furthermore, attempts have been made to predict the PRRT absorbed doses based on the pre-therapeutic ^{68}Ga-SSTR image (Stenvall et al. 2022, Bruvoll et al. 2023), which would subsequently promote a highly individualised PRRT treatment plan.

Hence, incorporating quantitative metrics for evaluating pre-therapeutic PET and peri-therapeutic SPECT imaging in the context of theragnostics shows interesting potential. However, evaluating quantitative metrics requires that phenomena impacting the quantitative accuracy are well understood, something the pipeline described in Chapter 6 may assist with.

8. Discussion and Future Outlook

Nuclear medicine imaging generates functional information non-invasively for disease diagnosis, assessment, and the personalisation of treatment strategies. Functional imaging is not limited to oncology; it is also an important tool in, for example, diagnosing cardiovascular disease and neurological disorders (Anand et al. 2009). The combination of anatomical imaging with functional imaging substantially enhances diagnostic capabilities, as it allows for evaluating the extent of the pathology while also providing an anatomical reference for the localisation of the disease.

Physiological images are commonly assessed qualitatively, which is often sufficient. However, qualitatively evaluating the disease to predict clinical behaviour, determine optimal treatment strategies, or assess therapeutic response can be challenging. This has led to a rise in the use of quantitative cancer biomarkers, and selecting therapeutic strategy based on biological tumour features has the potential to improve disease management (Meikle et al. 2021).

The use of cancer biomarkers as a prognostic or predictive indicator relies on defining quantitative thresholds to anticipate outcomes. The quantitative metrics one measures must be harmonised and highly reproducible to facilitate its translation into clinical practice (Boellaard 2009). While quantitative nuclear medicine imaging is appealing, achieving it in practice can be challenging.

What are then the metrics that one reliably can measure and use to define diagnostic thresholds? This question quickly shifts to additional questions regarding accuracy and precision, given the inherent difficulty in quantifying a radiopharmaceutical whose distribution changes over time and varies from patient to patient. Without great care, studies conducted on the same subject can exhibit large variations, and these variations are further exacerbated when considering different scanners, imaging protocols, and reconstruction algorithms (Meikle et al. 2021). Achieving consistent and unbiased assessment of tracer distribution and intensity is therefore paramount.

While significant advancements in nuclear medicine imaging have been achieved over the years, challenges such as motion, non-uniform and poor spatial resolution, and noise persist, and these are not necessarily easy to characterise. To address these limitations, Monte Carlo simulations can provide deeper insights into the phenomena that produce the observed data and its associated inaccuracies.

Additionally, Monte Carlo simulations can assist in optimising specific clinical objectives, such as improving image quality or reducing patient dose. In **Paper II**, Monte Carlo simulations were used to evaluate different activity-administration protocols to achieve a harmonised image quality, regardless of patient body size.

In this context, the theragnostic approach for management of NETs to diagnose and the subsequent PRRT treatment using radiopharmaceuticals with similar targeting mechanisms can potentially benefit from the use of quantitative biomarkers. However, the combination of pre-therapeutic and peri-therapeutic imaging, as in the case of [^{68}Ga]Ga-DOTA-TOC PET and [^{177}Lu]Lu-DOTA-TATE SPECT, presents challenges due to the involvement of different imaging modalities, radiopharmaceuticals, and imaging time points, which all contribute to the complexity of extrapolating prognostic and predictive clinical behaviour from one setting to the other. Consequently, it is important that one understands potential limitations that will affect accuracy and precision in the metrics to be determined, and in **Paper III**, Monte Carlo simulations were performed to evaluate the impact of respiration as a reason for one possible quantitative bias within the context of [^{68}Ga]Ga-DOTA-TOC PET and [^{177}Lu]Lu-DOTA-TATE SPECT.

There is a need to elevate our understanding of potential qualitative and quantitative limitations and inaccuracies within nuclear medicine exams, and MC simulations has the potential to facilitate this. However, it is important to emphasise that the constituents of the model should match the intricacy inherent in a clinical setting. In **Paper I**, substantial effort was introduced to certify that the pipeline is of similar complexity to its clinical scanner counterpart. If not, the assessment of the model's performance would be biased, and the data produced may not be clinically comparable. Following this, in **Paper IV**, efforts were made to improve the patient models so the intricacy of the patient models better correspond to the intricacy of an actual patient. With such improved models, one can systematically evaluate the effects of individual parameters to better grasp these biases. Going one step further, these models and simulations could allow for the creation of databases of simulated images with access to the ground truth. Such databases could be valuable in many aspects and can, as an example, be used to assess software performance and, in light of the rapid expansion of machine learning, as training data (Torres-Velazquez et al. 2021).

While the current pipeline in this thesis has been tailored towards oncological applications, and in particular, [^{68}Ga]Ga-DOTA-TOC PET, it is important to note that it can be extended to cover a wide range of radiopharmaceuticals and study protocols and, consequently, used to study other pathologies. As an example, PET can be used to evaluate ischemic heart disease qualitatively and quantitatively. Quantitative myocardial blood flow can be calculated with compartment models based on dynamic scans to estimate the kinetics of the tracer and, consequently, the myocardial blood flow (Sciagrà et al. 2021). In this case, the benefit of quantitative assessment lies in the potential to reveal balanced ischemias, which are not revealed

by semi-quantitative analysis. Notwithstanding, any biased estimate of activity concentration will result in a biased assessment of the myocardial blood flow. Hence, extending the pipeline to incorporate associated pharmacokinetic models for specific radiopharmaceuticals enables time-dependent activity distributions to be defined and used together with realistic patient models, which would promote its use in various clinical applications (Brolin et al. 2013). Consequently, the pipeline could then be used for various PET exams to systematically evaluate the impact of, e.g., respiratory and cardiac motion to better understand potential bias in quantitative estimates or as a means to evaluate the performance of analysis software and correction methods.

Ultimately, the extent to which clinical PET applications can be studied using the pipeline depends on the user's willingness to expand and improve the model's boundaries. However, when these modifications are in place, the simulations of tomorrow can facilitate answers *in silico* to questions that are difficult to separate *in vivo*.

9. Conclusions

The overarching objective of this thesis aimed to model and optimise ^{68}Ga-SSTR PET imaging with a focus towards theragnostic applications. A crucial aspect of this work involved creating a method that enables the simulation of a clinical PET scanner and the reconstruction of simulated data, entirely *in silico*. This is an important step, as nuclear medicine Monte Carlo simulation-based studies are seldom accompanied by a method to perform tomographic reconstruction. To ensure the reliability of the results, validating the pipeline was necessary, and the model was shown to produce results comparable to those obtained from a clinical scanner (**Paper I**), allowing for further simulation-based studies to be performed. Such an *in silico* pipeline offers flexibility to analyse various applications, such as assessing image quality under various conditions and simulating complex parameters like respiration, which is typically challenging in a clinical setting.

An illustration of the flexibility of the pipeline is demonstrated in **Papers II** and **III**, one assessing image quality when considering patient body size and activity-administration protocols in [^{68}Ga]Ga-DOTA-TOC PET exams (**Paper II**), and the other investigating potential quantitative bias due to respiration (**Paper III**) for the theragnostic pair [^{68}Ga]Ga-DOTA-TOC PET and [^{177}Lu]Lu-DOTA-TATE SPECT. Both studies underscore the benefits of Monte Carlo simulations, in which the construction of multiple instances of the same simulation geometry with slight variations are possible, and the access to the underlying data allows the generated results to be understood in the context of the study. This approach allows for the systematic evaluation of isolated parameters concerning the issue being investigated.

It is important to acknowledge the necessity of improving all constituents of the pipeline, including refinements of the patient model to better emulate the complexity of actual patients. If there is a mismatch in complexity between the simulation model and the actual exam, the performance assessment may be biased (**Paper IV**). Therefore, it is important to strive for refined patient-model realism in future simulation studies to extend the usability of the generated images, including, but not limited to, software performance assessment or their use in conjunction with machine learning.

As the final take-home message, this type of pipeline has proven its usefulness. It creates a controlled environment to test, optimise, and evaluate various aspects of the entire PET chain, from image acquisition to reconstruction. This reduces our dependence on physical scans and enhances our understanding of the impact of factors that are challenging to isolate *in vivo*. While the model is currently designed for ^{68}Ga-SSTR PET imaging, extending it to other radiopharmaceuticals is feasible, providing an opportunity to investigate other pathologies using this pipeline.

Acknowledgements

”Είναι πέτρα σαν τη καρδιά μου τη πληγωμένη
που κάτι να την μαλακώσει ανυπόμονα περιμένει.
Είναι ψαλίδι σαν τη χαρά που κόπηκε στη μέση
μα ακόμα ονειρεύομαι και ας μην τους αρέσει.
Είναι μολύβι σ'αυτό που το μυαλό μου βρίσκει διέξοδο
επάνω στο χαρτί έτσι ώστε να μη τρελαθεί.
Κυρίες και κύριοι αυτή είναι όλη μου η ζωή.
Είναι πέτρα, ψαλίδι, μολύβι, χαρτί.”

РФ

I would like to express my profound gratitude to the numerous individuals who have provided me with invaluable help and support throughout this journey.

To my main supervisor, Michael Ljungberg, I cannot thank you enough for your unwavering belief in me. You introduced me to the world of Monte Carlo simulations, a challenging yet rewarding journey that often had me pulling my hair out (do not get me started on those cryptic GATE errors). You allowed me to embark on a path to explore this field, and for that, I am truly grateful for the time and opportunity you have given me.

To my co-supervisor, Johan Gustafsson, I want to express my gratitude for your constant presence and tireless support. I would not be where I am today without your assistance. You have consistently guided me in the right direction, regardless of the subject, and I will always be grateful for your willingness to listen and to help.

To my co-supervisor, Cecilia Hindorf, I want to extend my gratitude for introducing the practical side of nuclear medicine. At some point, even I came to realise that there is a world beyond my computer screen, and your guidance have been invaluable for me to take that step.

I would like to thank my present and former colleagues at Medical Radiation Physics, Lund, and with a special thanks to the Nuclear Medicine group.

To my fellow PhD students, I want to express my gratitude for the times and laughter we have shared during lunches, breaks, and AWs (ett stort tack till AW-gruppen). A special shout-out to Elise, it appears as our time sharing an office is, at last, coming to a close. An extended *dose* of appreciation to Niccolò and Lovisa for the times we have shared supervising laboratory exercises.

Till min svenska και η ελληνική μου οικογένεια, we have a strange way of showing love, but I would not have it any other way. Μπαμπά, θέλω να σε ευχαριστήσω για όλα όσα έχεις κάνει για μένα. Μου έχεις δώσει ό,τι θα μπορούσα ποτέ να ζητήσω, υποστηρίζοντάς με σε όλη μου τη ζωή, πάντα ήσουν εκεί για μένα. Mamma, jag vill tacka för allt du har gjort för mig och för att du alltid har funnits där när jag behövt dig. Ditt stöd har varit ovärderliga och har format mig till den jag är idag. Nico, Ludvig, Iris, jag är oerhört tacksam för att ni är ni, och att ni är mina syskon.

Jag vill även tacka mina vänner för ert otroliga stöd och er vänskap. Ni har alltid funnits där för mig, och era *"råd"* och skratt har lyst upp mina dagar. Jag uppskattar er mer än ord kan beskriva.

References

Abdulrezzak, U., Kurt, Y. K., Kula, M. and Tutus, A. 2016. Combined imaging with 68Ga-DOTA-TATE and 18F-FDG PET/CT on the basis of volumetric parameters in neuroendocrine tumors. *Nucl Med Commun,* 37**,** 874-81.

Ackerman, M. J. 1998. The Visible Human Project. *Proceedings of the IEEE,* 86**,** 504-11.

Agostinelli, S., et al. 2003. GEANT4-a simulation toolkit. *Nucl Instrum Methods Phys Res A,* 506**,** 250-303.

Ahn, S. and Fessler, J. A. 2003. Globally convergent image reconstruction for emission tomography using relaxed ordered subsets algorithms. *IEEE Trans Med Imaging,* 22**,** 613-26.

Alqahtani, M. M., Willowson, K. P., Constable, C., Fulton, R. and Kench, P. L. 2022. Optimization of ^{99m}Tc whole-body SPECT/CT image quality: A phantom study. *J Appl Clin Med Phys,* 23.

Anand, S. S., Singh, H. and Dash, A. K. 2009. Clinical Applications of PET and PET-CT. *Med J Armed Forces India,* 65**,** 353-8.

Badawi, R. D. and Marsden, P. K. 1999. Developments in component-based normalization for 3D PET. *Phys Med Biol,* 44**,** 571-94.

Barrett, H. H. 1990. Objective Assessment of Image Quality - Effects of Quantum Noise and Object Variability. *J Opt Soc Am A,* 7**,** 1266-78.

Barrett, H. H., White, T. and Parra, L. C. 1997. List-mode likelihood. *J Opt Soc Am A,* 14**,** 2914-23.

Barrett, H. H., Wilson, D. W. and Tsui, B. M. W. 1994. Noise properties of the EM algorithm: I. Theory. *Phys Med Biol,* 39**,** 833-46.

Baum, R. P. and Kulkarni, H. R. 2012. THERANOSTICS: From Molecular Imaging Using Ga-68 Labeled Tracers and PET/CT to Personalized Radionuclide Therapy - The Bad Berka Experience. *Theranostics,* 2**,** 437-47.

Be, M. M., et al. 2004. Monographie BIPM-5, Vol.1, Bureau International des Poids et Mesures (2004).

Be, M. M., et al. 2013. Monographie BIPM-5, vol.7, Bureau International des Poids et Mesures (2013).

Bodei, L., Herrmann, K., Schoder, H., Scott, A. M. and Lewis, J. S. 2022. Radiotheranostics in oncology: current challenges and emerging opportunities. *Nat Rev Clin Oncol,* 19**,** 534-50.

Boellaard, R. 2009. Standards for PET image acquisition and quantitative data analysis. *J Nucl Med,* 50 Suppl 1**,** 11S-20S.

Brolin, G., et al. 2016. The accuracy of quantitative parameters in (99m)Tc-MAG3 dynamic renography: a national audit based on virtual image data. *Clin Physiol Funct Imaging,* 36**,** 146-54.

Brolin, G., Sjögreen Gleisner, K. and Ljungberg, M. 2013. Dynamic ^{99m}Tc-MAG3 renography: images for quality control obtained by combining pharmacokinetic modelling, an anthropomorphic computer phantom and Monte Carlo simulated scintillation camera imaging. *Phys Med Biol,* 58**,** 3145-61.

Bruvoll, R., Blakkisrud, J., Mikalsen, L. T., Connelly, J. and Stokke, C. 2023. Correlations between [^{68}Ga]Ga-DOTA-TOC Uptake and Absorbed Dose from [^{177}Lu]Lu-DOTA-TATE. *Cancers (Basel),* 15.

Bruyant, P. P. 2002. Analytic and iterative reconstruction algorithms in SPECT. *J Nucl Med,* 43**,** 1343-58.

Buchmann, I., et al. 2007. Comparison of 68Ga-DOTATOC PET and 111In-DTPAOC (Octreoscan) SPECT in patients with neuroendocrine tumours. *Eur J Nucl Med Mol Imaging,* 34**,** 1617-26.

Budinger, T. F. 1983. Time-of-flight positron emission tomography: status relative to conventional PET. *J Nucl Med,* 24**,** 73-8.

Buvat, I. and Castiglioni, I. 2002. Monte Carlo simulations in SPET and PET. *Q J Nucl Med,* 46**,** 48-61.

Caon, M. 2004. Voxel-based computational models of real human anatomy: a review. *Radiat Environ Biophys,* 42**,** 229-35.

Chen, Y. and Glick, S. J. 2007. Determination of the system matrix used in list-mode EM reconstruction of PET. *2007 IEEE Nuclear Science Symposium Conference Record, Honolulu***,** 3855-8.

Cherry, S. R. and Huang, S. C. 1995. Effects of Scatter on Model Parameter Estimates in 3d Pet Studies of the Human Brain. *IEEE Trans Nucl Sci,* 42**,** 1174-9.

Chicheportiche, A., Marciano, R. and Orevi, M. 2020. Comparison of NEMA characterizations for Discovery MI and Discovery MI-DR TOF PET/CT systems at different sites and with other commercial PET/CT systems. *EJNMMI Phys,* 7.

Colombino, P., Fiscella, B. and Trossi, L. 1965. Study of positronium in water and ice from 22 to -144 Degrees C by annihilation quanta measurements. *Il Nuovo Cimento,* 38.

Cristy, M. 1980. *Mathematical phantoms representing children of various ages for use in estimates of internal dose*. Oak Ridge National Lab. USA.

Daube-Witherspoon, M. E. and Cherry, S. R. 2021. Scanner design considerations for long axial field-of-view PET systems. *PET Clin,* 16**,** 25-39.

De Jong, H. W., Van Velden, F. H., Kloet, R. W., Buijs, F. L., Boellaard, R. and Lammertsma, A. A. 2007. Performance evaluation of the ECAT HRRT: an LSO-LYSO double layer high resolution, high sensitivity scanner. *Phys Med Biol,* 52**,** 1505-26.

De Man, B. and Basu, S. 2004. Distance-driven projection and backprojection in three dimensions. *Phys Med Biol,* 49**,** 2463-75.

De Pierro, A. R. and Yamagishi, M. E. B. 2001. Fast EM-like methods for maximum "a posteriori" estimates in emission tomography. *IEEE Trans Med Imaging,* 20**,** 280-8.

Dempster, A. P., Laird, N. M. and Rubin, D. B. 1977. Maximum Likelihood from Incomplete Data via the Em Algorithm. *J R Stat Soc Series B Stat Methodol,* 39**,** 1-38.

Deppen, S. A., et al. 2016. Safety and Efficacy of ^{68}Ga-DOTATATE PET/CT for Diagnosis, Staging, and Treatment Management of Neuroendocrine Tumors. *J Nucl Med,* 57**,** 708-14.

Derenzo, S. E., Budinger, T. F., Huesman, R. H., Cahoon, J. L. and Vuletich, T. 1981. Imaging Properties of a Positron Tomograph with 280 Bgo Crystals. *IEEE Trans Nucl Sci,* 28**,** 81-9.

Eckstein, M. P., Ahumada, A. J. and Watson, A. B. 1997. Visual signal detection in structured backgrounds. 2. Effects of contrast gain control, background variations, and white noise. *J Opt Soc Am A,* 14**,** 2406-19.

Eriksson, L., et al. 2007. An investigation of sensitivity limits in PET scanners. *Nucl Instrum Methods Phys Res A,* 580**,** 836-42.

Erlandsson, K., Buvat, I., Pretorius, P. H., Thomas, B. A. and Hutton, B. F. 2012. A review of partial volume correction techniques for emission tomography and their applications in neurology, cardiology and oncology. *Phys Med Biol,* 57**,** 119-59.

Fahey, F. H., Grogg, K. and El Fakhri, G. 2018. Use of Monte Carlo Techniques in Nuclear Medicine. *J Am Coll Radiol,* 15**,** 446-8.

Fani, M., et al. 2012. Unexpected Sensitivity of sst_2 Antagonists to N-Terminal Radiometal Modifications. *J Nucl Med,* 53**,** 1481-9.

Fani, M., et al. 2011. PET of Somatostatin Receptor-Positive Tumors Using ^{64}Cu- and ^{68}Ga-Somatostatin Antagonists: The Chelate Makes the Difference. *J Nucl Med,* 52**,** 1110-8.

Fendler, W. P., et al. 2017. ^{68}Ga-DOTATATE PET/CT Interobserver Agreement for Neuroendocrine Tumor Assessment: Results of a Prospective Study on 50 Patients. *J Nucl Med,* 58**,** 307-11.

Filipović, M., Comtat, C. and Stute, S. 2019. Time-of-flight (TOF) implementation for PET reconstruction in practice. *Phys Med Biol,* 64.

Frangos, S. and Buscombe, J. R. 2019. Why should we be concerned about a "g"? *Eur J Nucl Med Mol Imaging,* 46**,** 519.

Frey, E. C. and Tsui, B. M. W. 2006. Analytical Image Reconstruction Methods in Emisssion Computed Tomography. *In:* Zaidi, H. (ed.) *Quantitative Analysis in Nuclear Medicine Imaging.* New York, USA: Springer.

Fu, W., Sturgeon, G. M., Agasthya, G., Segars, W. P., Kapadia, A. J. and Samei, E. 2017. Breast dose reduction with organ-based, wide-angle tube current modulated CT. *J Med Imaging (Bellingham),* 4.

Gaitanis, A., Kontaxakis, G., Spyrou, G., Panayiotakis, G. and Tzanakos, G. 2010. PET image reconstruction: A stopping rule for the MLEM algorithm based on properties of the updating coefficients. *Comput Med Imaging Graph,* 34**,** 131-41.

Geijer, H. and Breimer, L. H. 2013. Somatostatin receptor PET/CT in neuroendocrine tumours: update on systematic review and meta-analysis. *Eur J Nucl Med Mol Imaging,* 40**,** 1770-80.

Germano, G. and Hoffman, E. J. 1990. A study of data loss and mispositioning due to pileup in 2-D detectors in PET. *IEEE Trans Nucl Sci,* 37**,** 671-5.

Gonzalez-Montoro, A., Ullah, M. N. and Levin, C. S. 2022. Advances in Detector Instrumentation for PET. *J Nucl Med,* 63**,** 1138-44.

Graham, M. M., Gu, X. M., Ginader, T., Breheny, P. and Sunderland, J. J. 2017. ^{68}Ga-DOTATOC Imaging of Neuroendocrine Tumors: A Systematic Review and Metaanalysis. *J Nucl Med,* 58**,** 1452-8.

Hennrich, U. and Benesova, M. 2020. [^{68}Ga]Ga-DOTA-TOC: The First FDA-Approved ^{68}Ga-Radiopharmaceutical for PET Imaging. *Pharmaceuticals (Basel),* 13.

Herrmann, K., et al. 2020. Radiotheranostics: a roadmap for future development. *Lancet Oncol,* 21**,** 146-56.

Hoffman, E. J., Guerrero, T. M., Germano, G., Digby, W. M. and Dahlbom, M. 1989. PET system calibrations and corrections for quantitative and spatially accurate images. *IEEE Trans Nucl Sci,* 36**,** 1108-12.

Hoffman, E. J., Huang, S. C., Phelps, M. E. and Kuhl, D. E. 1981. Quantitation in positron emission computed tomography: 4. Effect of accidental coincidences. *J Comput Assist Tomogr,* 5**,** 391-400.

Hudson, H. M. and Larkin, R. S. 1994. Accelerated image reconstruction using ordered subsets of projection data. *IEEE Trans Med Imaging,* 13**,** 601-9.

Hutton, B., Nuyts, J. and Zaidi, H. 2006. Iterative Reconstruction Methods. *In:* Zaidi, H. (ed.) *Quantitative Analysis in Nuclear Medicine Imaging.* Boston, USA: Springer.

Iatrou, M., Manjeshwar, R. M., Ross, S. G., Thielemans, K. and Stearns, C. W. 2006. 3D implementation of Scatter Estimation in 3D PET. *Nuclear Science Symposium Conference Record.*

ICRU 1984. *ICRU Report 37 - Stopping Powers for Electrons and Positrons*. International Commission on Radiation Units and Measurements. Bethesda, USA.

ICRU 1992. *ICRU Report 48 - Phantoms and Computational Models in Therapy, Diagnosis and Protection*. International Commission on Radiation Units and Measurements. Bethesda, USA.

James, F. 1994. RANLUX: A Fortran implementation of the high-quality pseudorandom number generator of Lüscher. *Comput Phys Commun,* 79**,** 111-4.

Jan, S., et al. 2004. GATE: a simulation toolkit for PET and SPECT. *Phys Med Biol,* 49**,** 4543-61.

Joseph, P. M. 1982. An Improved Algorithm for Reprojecting Rays Through Pixel Images. *IEEE Trans Med Imaging,* 1**,** 192-6.

Kainz, W., et al. 2019. Advances in Computational Human Phantoms and Their Applications in Biomedical Engineering-A Topical Review. *IEEE Trans Radiat Plasma Med Sci,* 3**,** 1-23.

Kak, A. and Slaney, M. 1988. *Principles of Computerized Tomographic Imaging*, IEEE Press.

Kamphuis, C., Beekman, F. J. and Viergever, M. A. 1996. Evaluation of OS-EM vs. ML-EM for 1D, 2D and fully 3D SPECT reconstruction. *IEEE Trans Nucl Sci,* 43**,** 2018-24.

Kessler, R. M., Ellis, J. R., Jr. and Eden, M. 1984. Analysis of emission tomographic scan data: limitations imposed by resolution and background. *J Comput Assist Tomogr,* 8**,** 514-22.

Kim, C. H., Jeong, J. H., Bolch, W. E., Cho, K. W. and Hwang, S. B. 2011. A polygon-surface reference Korean male phantom (PSRK-Man) and its direct implementation in Geant4 Monte Carlo simulation. *Phys Med Biol,* 56**,** 3137-61.

Kinahan, P. E., et al. 2020. The QIBA Profile for FDG PET/CT as an Imaging Biomarker Measuring Response to Cancer Therapy. *Radiology,* 294**,** 647-57.

Kojima, A., Matsumoto, M., Takahashi, M., Hirota, Y. and Yoshida, H. 1989. Effect of spatial resolution on SPECT quantification values. *J Nucl Med,* 30**,** 508-14.

Kratochwil, C., et al. 2015. SUV of [^{68}Ga]DOTATOC-PET/CT Predicts Response Probability of PRRT in Neuroendocrine Tumors. *Mol Imaging Biol,* 17**,** 313-8.

Lammertsma, A. A. 2017. Forward to the Past: The Case for Quantitative PET Imaging. *J Nucl Med,* 58**,** 1019-24.

Lange, K. and Carson, R. 1984. EM reconstruction algorithms for emission and transmission tomography. *J Comput Assist Tomogr,* 8**,** 306-16.

Leahy, R. M. and Qi, J. Y. 2000. Statistical approaches in quantitative positron emission tomography. *Stat Comput,* 10**,** 147-65.

Lecoq, P., et al. 2020. Roadmap toward the 10 ps time-of-flight PET challenge. *Phys Med Biol,* 65.

Lecuyer, P. 1988. Efficient and Portable Combined Random Number Generators. *Commun ACM,* 31.

Lee, C., Lodwick, D., Hasenauer, D., Williams, J. L., Lee, C. and Bolch, W. E. 2007. Hybrid computational phantoms of the male and female newborn patient: NURBS-based whole-body models. *Phys Med Biol,* 52**,** 3309-33.

Lee, I., et al. 2015. Comparison of Diagnostic Sensitivity and Quantitative Indices Between ^{68}Ga-DOTATOC PET/CT and ^{111}In-Pentetreotide SPECT/CT in Neuroendocrine Tumors: a Preliminary Report. *Nucl Med Mol Imaging,* 49**,** 284-90.

Levin, C. S. and Hoffman, E. J. 1999. Calculation of positron range and its effect on the fundamental limit of positron emission tomography system spatial resolution. *Phys Med Biol,* 44**,** 781-99.

Liow, J. S. and Strother, S. C. 1993. The convergence of object dependent resolution in maximum likelihood based tomographic image reconstruction. *Phys Med Biol,* 38**,** 55-70.

Ljungberg, M. 2012. The SIMIND Monte Carlo Code. *In:* Ljungberg, M., Strand, S. E. & King, M. A. (eds.) *Monte Carlo Calculation in Nuclear Medicine: Applications in Diagnostic Imaging - second edition.*: CRC Press.

Ljungberg, M. and Strand, S. E. 1989. A Monte Carlo program for the simulation of scintillation camera characteristics. *Comput Methods Programs Biomed,* 29**,** 257-72.

Lois, C., et al. 2010. An assessment of the impact of incorporating time-of-flight information into clinical PET/CT imaging. *J Nucl Med,* 51**,** 237-45.

Lyra, M. and Ploussi, A. 2011. Filtering in SPECT Image Reconstruction. *Int J Biomed Imaging*.

Matsumoto, M. and Nishimura, T. 1998. Mersenne twister: a 623-dimensionally equidistributed uniform pseudo-random number generator. *ACM Trans Model Comput Simul,* 8**,** 3-30.

Meikle, S. R. and Badawi, R. D. 2005. Quantitative Techniques in PET. *Positron Emission Tomography.* London: Springer.

Meikle, S. R., Kench, P., Kassiou, M. and Banati, R. B. 2005. Small animal SPECT and its place in the matrix of molecular imaging technologies. *Phys Med Biol,* 50.

Meikle, S. R., et al. 2021. Quantitative PET in the 2020s: a roadmap. *Phys Med Biol,* 66.

Merlin, T., et al. 2018. CASToR: a generic data organization and processing code framework for multi-modal and multi-dimensional tomographic reconstruction. *Phys Med Biol,* 63.

Miller, C., Rousseau, J., Ramogida, C. F., Celler, A., Rahmim, A. and Uribe, C. F. 2022. Implications of physics, chemistry and biology for dosimetry calculations using theranostic pairs. *Theranostics,* 12**,** 232-59.

Mittra, E. S. 2018. Neuroendocrine Tumor Therapy: ^{177}Lu-DOTATATE. *AJR Am J Roentgenol,* 211**,** 278-85.

Moses, W. W. 2011. Fundamental Limits of Spatial Resolution in PET. *Nucl Instrum Methods Phys Res A***,** 236-40.

Nagtegaal, I. D., et al. 2020. The 2019 WHO classification of tumours of the digestive system. *Histopathology,* 76**,** 182-8.

Oddstig, J., Brolin, G., Trägårdh, E. and Minarik, D. 2021. Head-to-head comparison of a Si-photomultiplier-based and a conventional photomultiplier-based PET-CT system. *EJNMMI Phys,* 8**,** 19.

Ollinger, J. M. 1996. Model-based scatter correction for fully 3D PET. *Phys Med Biol,* 41**,** 153-76.

Oronsky, B., Ma, P. C., Morgensztern, D. and Carter, C. A. 2017. Nothing But NET: A Review of Neuroendocrine Tumors and Carcinomas. *Neoplasia,* 19**,** 991-1002.

Panin, V. Y., Kehren, F., Rothfuss, H., Hu, D., Michel, C. and Casey, M. E. 2006. PET reconstruction with system matrix derived from point source measurements. *IEEE Trans Nucl Sci,* 53**,** 152-9.

Pretorius, P. H., Liu, C., Fan, P., Peterson, M. and Ljungberg, M. 2015. Monte Carlo Simulations of the GE Discovery Alcyone CZT SPECT Systems. *IEEE Trans Nucl Sci,* 62**,** 832-9.

Qi, J. and Leahy, R. M. 2006. Iterative reconstruction techniques in emission computed tomography. *Phys Med Biol,* 51**,** R541-78.

Qi, J., Leahy, R. M., Cherry, S. R., Chatziioannou, A. and Farquhar, T. H. 1998. High-resolution 3D Bayesian image reconstruction using the microPET small-animal scanner. *Phys Med Biol,* 43**,** 1001-13.

Rahmim, A., Qi, J. and Sossi, V. 2013. Resolution modeling in PET imaging: theory, practice, benefits, and pitfalls. *Med Phys,* 40.

Rahmim, A. and Zaidi, H. 2008. PET versus SPECT: strengths, limitations and challenges. *Nucl Med Commun,* 29**,** 193-207.

Reader, A. J., Erlandsson, K., Flower, M. A. and Ott, R. J. 1998. Fast accurate iterative reconstruction for low-statistics positron volume imaging. *Phys med Biol,* 43**,** 835-46.

Reader, A. J., Julyan, P. J., Williams, H., Hastings, D. L. and Zweit, J. 2003. EM algorithm system modeling by image-space techniques for PET reconstruction. *IEEE Trans Nucl Sci,* 50**,** 1392-7.

Reubi, J. C. and Schonbrunn, A. 2013. Illuminating somatostatin analog action at neuroendocrine tumor receptors. *Trends Pharmacol Sci,* 34**,** 676-88.

Rolland, J. P. and Barrett, H. H. 1992. Effect of Random Background Inhomogeneity on Observer Detection Performance. *J Opt Soc Am A,* 9**,** 649-58.

Roth, D., Larsson, E., Ljungberg, M. and Sjögreen Gleisner, K. 2022. Monte Carlo modelling of a compact CZT-based gamma camera with application to ^{177}Lu imaging. *EJNMMI Phys,* 9**,** 35.

Sanchez-Crespo, A. 2013. Comparison of Gallium-68 and Fluorine-18 imaging characteristics in positron emission tomography. *Appl Radiat Isot,* 76**,** 55-62.

Sanli, Y., Garg, I., Kandathil, A., Kendi, T., Zanetti, M. J. B., Kuyumcu, S. and Subramaniam, R. M. 2018. Neuroendocrine Tumor Diagnosis and Management: ^{68}Ga-DOTATATE PET/CT. *AJR Am J Roentgenol,* 211**,** 267-77.

Sarrut, D. and Guigues, L. 2008. Region-oriented CT image representation for reducing computing time of Monte Carlo simulations. *Med Phys,* 35**,** 1452-63.

Schurr, P. G., et al. 2007. Aggressive surgery improves long-term survival in neuroendocrine pancreatic tumors - An institutional experience. *Ann Surg,* 245**,** 273-81.

Sciagrà, R., et al. 2021. EANM procedural guidelines for PET/CT quantitative myocardial perfusion imaging. *Eur J Nucl Med Mol Imaging,* 48**,** 1040-69.

Segars, W. P., et al. 2013. Population of anatomically variable 4D XCAT adult phantoms for imaging research and optimization. *Med Phys,* 40.

Segars, W. P., Sturgeon, G., Mendonca, S., Grimes, J. and Tsui, B. M. W. 2010. 4D XCAT phantom for multimodality imaging research. *Med Phys,* 37**,** 4902-15.

Sempau, J., Acosta, E., Baro, J., Fernández-Varea, J. M. and Salvat, F. 1997. An algorithm for Monte Carlo simulation of coupled electron-photon transport. *Nucl Instrum Methods Phys Res B,* 132**,** 377-90.

Shepp, L. A. and Logan, B. F. 1974. The Fourier Reconstruction of a Head Section. *IEEE Trans Nucl Sci*.

Siddon, R. L. 1985. Fast calculation of the exact radiological path for a three-dimensional CT array. *Med Phys,* 12**,** 252-5.

Snyder, W., Ford, M. and Warner, G. 1978. MIRD Pamphlet No 5: Estimates of specific absorbed fractions for photon sources uniformly distributed in various organs of a heterogeneous phantom. Society of Nuclear Medicine. New York.

Soret, M., Bacharach, S. L. and Buvat, I. 2007. Partial-volume effect in PET tumor imaging. *J Nucl Med,* 48**,** 932-45.

Srinivas, S. M., Dhurairaj, T., Basu, S., Bural, G., Surti, S. and Alavi, A. 2009. A recovery coefficient method for partial volume correction of PET images. *Ann Nucl Med,* 23**,** 341-8.

Stabin, M. G., et al. 1995. *Mathematical models and specific absorbed fractions of photon energy in the nonpregnant adult female and at the end of each trimester of pregnancy*. Oak Ridge National Lab. USA.

Stenvall, A., et al. 2022. Relationships between uptake of [^{68}Ga]Ga-DOTA-TATE and absorbed dose in [^{177}Lu]Lu-DOTA-TATE therapy. *EJNMMI Res,* 12**,** 75.

Stute, S. and Comtat, C. 2013. Practical considerations for image-based PSF and blobs reconstruction in PET. *Phys Med Biol,* 58**,** 3849-70.

Sundlöv, A. and Sjögreen Gleisner, K. 2021. Peptide Receptor Radionuclide Therapy - Prospects for Personalised Treatment. *Clinical Oncology (R Coll Radiol),* 33**,** 92-7.

Surti, S. 2015. Update on time-of-flight PET imaging. *J Nucl Med,* 56**,** 98-105.

Surti, S., Scheuermann, R. and Karp, J. S. 2009. Correction technique for cascade gammas in I-124 imaging on a fully-3D, Time-of-Flight PET Scanner. *IEEE Trans Nucl Sci,* 56**,** 653-60.

Thielemans, K., Manjeshwar, R. M., Tsoumpas, C. and Jansen, F. P. 2007. A new algorithm for scaling of PET scatter estimates using all coincidence events. *2007 IEEE Nuclear Science Symposium Conference Record*.

Thielemans, K., Tsoumpas, C., Mustafovic, S., Beisel, T., Aguiar, P., Dikaios, N. and Jacobson, M. W. 2012. STIR: software for tomographic image reconstruction release 2. *Phys Med Biol,* 57**,** 867-83.

Tirosh, A., et al. 2018. Prognostic Utility of Total ^{68}Ga-DOTATATE-Avid Tumor Volume in Patients With Neuroendocrine Tumors. *Gastroenterology,* 154**,** 998-1008.

Tong, S., Alessio, A. M., Thielemans, K., Stearns, C., Ross, S. and Kinahan, P. E. 2011. Properties and Mitigation of Edge Artifacts in PSF-Based PET Reconstruction. *IEEE Trans Nucl Sci,* 58**,** 2264-75.

Toriihara, A., et al. 2019. Prognostic value of somatostatin receptor expressing tumor volume calculated from ^{68}Ga-DOTATATE PET/CT in patients with well-differentiated neuroendocrine tumors. *Eur J Nucl Med Mol Imaging,* 46**,** 2244-51.

Torres-Velazquez, M., Chen, W. J., Li, X. and Mcmillan, A. B. 2021. Application and Construction of Deep Learning Networks in Medical Imaging. *IEEE Trans Radiat Plasma Med Sci,* 5**,** 137-59.

Tsoli, M., Chatzellis, E., Koumarianou, A., Kolomodi, D. and Kaltsas, G. 2019. Current best practice in the management of neuroendocrine tumors. *Ther Adv Endocrinol Metab,* 10.

Tsui, B. M., Frey, E. C., Zhao, X., Lalush, D. S., Johnston, R. E. and Mccartney, W. H. 1994. The importance and implementation of accurate 3D compensation methods for quantitative SPECT. *Phys Med Biol,* 39**,** 509-30.

Veklerov, E. and Llacer, J. 1987. Stopping Rule for the MLE Algorithm Based on Statistical Hypothesis Testing. *IEEE Trans Med Imaging,* 6**,** 313-9.

Veklerov, E., Llacer, J. and Hoffman, E. J. 1988. MLE reconstruction of a brain phantom using a Monte Carlo transition matrix and a statistical stopping rule. *IEEE Trans Nucl Sci,* 35**,** 603-7.

Wagadarikar, A. A., Ivan, A., Dolinsky, S. and Mcdaniel, D. L. 2014. Sensitivity Improvement of Time-of-Flight (ToF) PET Detector Through Recovery of Compton Scattered Annihilation Photons. *IEEE Trans Nucl Sci,* 61**,** 121-5.

Wagatsuma, K., et al. 2017. Comparison between new-generation SiPM-based and conventional PMT-based TOF-PET/CT. *Phys Med,* 42**,** 203-10.

Watson, C. C. 2007. Extension of Single Scatter Simulation to Scatter Correction of Time-of-Flight PET. *IEEE Trans Nucl Sci,* 54**,** 1679-86.

Werling, A., Bublitz, O., Doll, J., Adam, L. E. and Brix, G. 2002. Fast implementation of the single scatter simulation algorithm and its use in iterative image reconstruction of PET data. *Phys Med Biol,* 47**,** 2947-60.

Werner, R. A., et al. 2018. SSTR-RADS Version 1.0 as a Reporting System for SSTR PET Imaging and Selection of Potential PRRT Candidates: A Proposed Standardization Framework. *J Nucl Med,* 59**,** 1085-91.

Wettenhovi, V. V., Vauhkonen, M. and Kolehmainen, V. 2021. OMEGA-open-source emission tomography software. *Phys Med Biol,* 66.

Wilson, D. W., Tsui, B. M. and Barrett, H. H. 1994. Noise properties of the EM algorithm: II. Monte Carlo simulations. *Phys Med Biol,* 39**,** 847-71.

Wilson, D. W. and Tsui, B. M. W. 1993. Noise Properties of Filtered-Backprojection and Ml-Em Reconstructed Emission Tomographic-Images. *IEEE Trans Nucl Sci,* 40**,** 1198-1203.

Zaidi, H. 1999. Relevance of accurate Monte Carlo modeling in nuclear medical imaging. *Med Phys,* 26**,** 574-608.

Zaidi, H. 2022. Monte Carlo techniques in nuclear medicine dosimetry. *In:* Zaidi, H. (ed.) *Monte Carlo Calculations in Nuclear Medicine.* 2 ed.: IOP Publishing.

Zhang, Y. K., Li, X., Segars, W. P. and Samei, E. 2014. Comparison of patient specific dose metrics between chest radiography, tomosynthesis, and CT for adult patients of wide ranging body habitus. *Med Phys,* 41.

Zubal, I. G., Harrell, C. R., Smith, E. O., Rattner, Z., Gindi, G. and Hoffer, P. B. 1994. Computerized three-dimensional segmented human anatomy. *Med Phys,* 21**,** 299-302.

Printed by Tryckeriet i E-huset, Lund 2023

LUND
UNIVERSITY

Medical Radiation Physics, Lund
Faculty of Science
ISBN 978-91-8039-879-4 (print)
ISBN 978-91-8039-878-7 (electronic)